05.01.2016, accepted for publication in *Coastal Engineering* 109(3), 20-41 (doi:10.1016/j.coastaleng.2015.12.004)

Composite modelling of subaerial landslide-tsunamis in different water body geometries and novel insight into slide and wave kinematics

Valentin Heller[1,2,*], Mark Bruggemann[2], Johannes Spinneken[2] and Benedict D. Rogers[3]

[1]Geohazards and Earth Processes Research Group, Faculty of Engineering, University of Nottingham, Nottingham NG7 2RD, UK

[2]Department of Civil and Environmental Engineering, Imperial College London, London SW7 2AZ, UK

[3]School of Mechanical, Aerospace and Civil Engineering, University of Manchester, Manchester M13 9PL, UK

*Corresponding author: Tel.: +44 1157 486 049.

E-mail addresses: Valentin.heller@nottingham.ac.uk (V. Heller), Mark.bruggemann08@imperial.ac.uk (M. Bruggemann), J.spinneken@imperial.ac.uk (J. Spinneken), Benedict.rogers@manchester.ac.uk (B.D. Rogers).

Abstract

This article addresses subaerial landslide-tsunamis with a composite (experimental-numerical) modelling approach. A shortcoming of generic empirical equations used for hazard assessment is that they are commonly based on the two idealised water body geometries of a wave channel (2D) or a wave basin (3D). A recent systematic comparison of 2D and 3D physical block model tests revealed wave amplitude differences of up to a factor of 17. The present article investigates two of these recently presented 2D-3D test pairs in detail, involving a solitary-like wave (scenario 1) and Stokes-like waves (scenario 2). Results discussed include slide and water particle kinematics and novel pressure measurements on the slide front. Instantaneous slide-water interaction power graphs are derived and potential and

kinetic wave energies are analysed. Solitary wave theory is found most appropriate to describe the wave kinematics associated with scenario 1, whereas Stokes theory accurately describes the tsunami in scenario 2. The data of both scenarios are further used to calibrate the smoothed particle hydrodynamics (SPH) code DualSPHysics v3.1, which includes a discrete element method (DEM)-based model to simulate the slide-ramp interaction. Five intermediate geometries, lying between the ideal 2D and 3D cases, are then investigated purely numerically. For a "channel" geometry with a diverging side wall angle of 7.5°, the wave amplitudes along the slide axes were found to lie approximately halfway between the values observed in 2D and 3D. At 45°, the amplitudes are practically identical to those in 3D. The study finally discusses the implications of the findings for engineering applications and illustrates the potential and current limitations of DualSPHysics for landslide-tsunami hazard assessment.

Keywords: Composite modelling; Fluid-Structure interaction; Impulse wave; Landslide-tsunami; Smoothed Particle Hydrodynamics; SPH.

1 Introduction

1.1 Overview

1.1.1 Relevance

Landslide-tsunamis (impulse waves) are caused by mass movements such as landslides, rockfalls, snow avalanches, ice calvings or asteroids interacting with a water body. Such waves are commonly referred to as tsunamis in an open ocean and as impulse waves in more restricted water bodies such as fjords, lakes or reservoirs. Extreme examples include the 1958 Lituya Bay case with a run-up height of 524 m (Miller, 1960) and the 1963 Vajont case where an impulse wave overtopped a dam by approximately 70 m resulting in around 2,000

casualties (Müller, 1964). Landslide-tsunamis and impulse waves occur quite frequently, at least on a smaller scale. In Switzerland, for example, the risk of several potential cases needed to be assessed within recent years. This included a case in Lake Lucerne, where in 2007 a rockslide caused an impulse wave and the risk of a future potential event had to be assessed (Fuchs and Boes, 2010), as well as a case where a snow avalanche may impact into an alpine lake. These examples were observed in a small country with 45 dam reservoirs larger than 10 million m^3 (Wikipedia, 2015a). Such threats occur much more frequently on a global scale, considering countries and regions such as China, with more than 87,000 dams (International Rivers, 2015), Norway, with 1,190 fjords (Wikipedia, 2015b), and Greenland, where ice calving may be observed every few minutes (personal communication, Esben Christiansen, Greenland).

1.1.2 Hazard assessment methods

Landslide-tsunami waves are mainly mitigated with passive methods including early warning, evacuation, reinforced infrastructure, safety clearance from ice calving prone areas, reservoir drawdown or provision of adequate freeboard of dam reservoirs. Such methods require detailed knowledge of the wave features, which are essentially obtained through three methods:

(i) Generic empirical equations derived from physical and/or numerical model tests,

(ii) Case-specific numerical simulations, and

(iii) Case-specific physical model tests.

In method (i), the unknown wave parameters are expressed through generic empirical equations as a function of the slide impact characteristics (slide properties, hill slope angle, water depth) and the wave propagation parameters (distance from the source, propagation direction). To obtain the underlying empirical equations, the slide characteristics have been

systematically varied in a number of subaerial landslide studies. This includes a substantial body of research conducted in wave channels (2D) (Noda, 1970; Wiegel et al., 1970; Kamphuis and Bowering, 1972; Slingerland and Voight, 1979; Huber and Hager, 1997; Monaghan et al., 2003; Walder et al., 2003; Fritz et al., 2004; Quecedo et al., 2004; Liu et al., 2005; Lynett and Liu, 2005; Zweifel et al., 2006; Ataie-Ashtiani and Nik-Khah, 2008; Heller et al., 2008; Abadie et al., 2010; Heller and Hager, 2010, 2011, 2014; Fuchs et al., 2013; Heller and Spinneken, 2013, 2015) with fewer studies undertaken in wave basins (3D) (Huber and Hager, 1997; Panizzo et al., 2005; Mohammed and Fritz, 2012; Heller and Spinneken, 2015). All of the above studies are based on idealisations including a horizontal bottom, a fully-granular or fully-rigid slide, as well as wave generation and propagation in either 2D or 3D. Section 1.1.3 provides further discussion as to how these idealisations relate to real-world cases. A selection of empirical equations for wave generation, propagation, run-up and forces on dams were combined in Heller et al. (2009), allowing for an efficient preliminary hazard assessment at low cost, within a short time frame (hours, days) and with minor resources (Fuchs and Boes, 2010; BGC, 2012; Cannata et al., 2012; Battaglia et al., 2015). As a result, method (i) is often considered sufficient in engineering practice. However, if method (i) predicts a wave run-up which is close to or in excess of a critical limit (e.g. the freeboard at a dam), or the water body geometry and/or bathymetry are complex, then a more detailed investigation relying on methods (ii) or (iii) is recommended.

In method (ii), a numerical code is validated and calibrated and subsequently applied to a specific case (Ward and Day, 2003; Løvholt et al., 2008; Abadie et al., 2012). This method may result in more accurate predictions than method (i); however, it requires more skills, time (weeks to months) and resources. Fortunately, these disadvantages have been substantially reduced in recent years: numerical solvers based as smoothed particle hydrodynamics (SPH) or Volume-of-Fluid (VOF) methods may now be able to cope with violent multi-phase/multi-

material free-surface flows, computational power has increased steadily, more efficient computing resources such as graphics processing units (GPUs) are utilised, freely available open source packages have emerged, and user friendly pre- and post-processing tools are being developed. The application of such numerical codes is no longer restricted to highly skilled numerical modellers, and engineering problems may now be tackled (Crespo et al., 2015).

At present, the most accurate method in landslide-tsunami and impulse wave hazard assessment is method (iii), a case-specific physical model study (Fuchs et al., 2011; WCHL, 1970). The geometry and bathymetry can be reproduced in great detail such that accurate results may be expected for a given slide scenario, provided that the model size is sufficiently large to rule out significant scale effects (Heller et al., 2008) and an appropriate slide model is selected. Disadvantages of method (iii) are that significant resources (laboratory space, measurement equipment) are required and that a typical time frame for an investigation exceeds one year. A main aim of the present study is to support and improve the two less expensive hazard assessment methods (i) and (ii).

1.1.3 Relevance of the effect of the water body geometry

A shortcoming of method (i) is that it is commonly based on the idealised water body geometries wave channel (2D) or wave basin (3D). Both geometries have their justification in real-world applications, and may be considered as two extreme cases of naturally occurring geometries (Heller et al., 2009):

(I) 2D (line source): the slide impacts longitudinally, the slide (subscript s) width b_s being identical or larger than the water body width b. The waves are confined as they move along x, the longitudinal direction of the water body without transverse or radial spreading.

(II) 3D (point source): the slide, with a width $b_s < b$, impacts into a larger water body. The waves propagate laterally and radially from the slide impact zone and can be described in cylindrical coordinates with the radial distance r and the wave propagation angle γ.

The physical understanding of the effect of the water body geometry on landslide-tsunamis and impulse waves is relatively limited. To address this, Heller and Spinneken (2015) (hereafter referred to as HS15) reviewed the most significant contributions to this field (Kranzer and Keller, 1959; Chang et al., 1979; Jiang and LeBlond, 1994; Huber and Hager, 1997; Watts et al., 2005; Heller et al., 2009, 2012), and systematically compared 2D and 3D physical model tests. These latter 2D-3D tests were conducted under identical conditions (slides, slide impact velocities) and showed that the waves decay with $x^{-0.30}$ and $r^{-1.0}$ in 2D and 3D, respectively. HS15 observed four wave types in 2D, whereas only the two least non-linear types occur in 3D. Furthermore, for a large slide Froude number F, relative slide thickness S and relative slide mass M, the 3D wave heights in the slide impact zone can be as large as in 2D. However, 3D and 2D wave heights along the slide axis differ for small F, S and M by up to a factor of 2.7 in the near-field, and typically by an order of magnitude in the far-field. HS15 also presented a novel methodology to transform data obtained from 2D to 3D. Not covered in HS15 were intermediate geometries between 2D and 3D, and the so-called 3D corner case (3Dc) where the slide impacts in the corner of a basin, similarly as in the potential impulse wave in the Kühtai reservoir in Austria (Fuchs et al., 2011; Heller et al., 2012).

In seeking to enhance our physical understanding of the processes involved in landslide-tsunami generation and propagation, the present paper investigates two distinct 2D-3D test pairs of HS15 in significantly more detail; this being primarily based on unpublished measurements of slide impact pressures and fluid kinematics. These test pairs involve weakly-dispersive (scenario 1) and strongly-dispersive (scenario 2) waves. These data are

subsequently used to calibrate and validate a numerical code, and to numerically investigate waves in intermediate geometries.

1.1.4 Numerical modelling

Subaerial landslide-tsunamis are a major challenge for Computational Fluid Dynamics due to high-speed slide impacts, multi-phases/multi-materials and complex free water surfaces. Suitable numerical models for subaerial landslide-tsunami predictions include higher-order Boussinesq models (e.g. Fuhrman and Madsen, 2009), Reynolds Averaged Navier-Stokes Equation models (e.g. Bascarini, 2010), Large Eddy Simulations (e.g. Liu et al., 2005) and Direct Numerical Simulation (e.g. Abadie et al., 2010). In these studies, the free surface is often tracked and located such as with the Volume-of-Fluid (VOF) method (e.g. Heinrich, 1992; Abadie et al., 2010). The challenges of tracking the free surface are reduced in the increasingly popular SPH method (e.g. Ataie-Ashtiani and Shobeyri, 2008; Rogers and Dalrymple, 2008; Yim et al., 2008; Capone et al., 2010).

SPH is a mesh-free Lagrangian method first devised in the 1970s for simulating astrophysical problems (Gingold and Monaghan, 1977; Gómez-Gesteira et al., 2010). The first attempt to apply the method to free-surface flows was undertaken by Monaghan (1994), where it was understood that, in contrast to most other numerical methods, SPH requires no explicit treatment of the free water surface (Dalrymple and Rogers, 2006). Furthermore, SPH can inherently deal with bi-phasic problems with a low density ratio (Fourtakas et al., 2013). These key advantages make SPH very popular in landslide-tsunami simulations, where impact craters and air entrainment can be important factors (Ataie-Ashtiani Shobeyri, 2008; Yim et al., 2008). The suitability of SPH to model landslide-tsunamis is further investigated in the present study, relying upon the recently released SPH open source code DualSPHysics v3.1 (Crespo et al., 2015).

1.2 Aims of the present article

Based on the above discussion, this article aims to supports the tsunami hazard assessment methods (i) and (ii) described in Section 1.1.2, with the following sub-aims:

(a) Provide new physical insight into slide-water interaction power, slide energy, wave energy and wave kinematics based on novel, high quality measurements and theoretical analysis,

(b) Investigate the potential of the open source code DualSPHysics v3.1 for subaerial landslide-tsunami hazard assessment in the context of method (ii), and

(c) Enhance the physical understanding of the effect of the water body geometry through numerical simulations of waves propagating in intermediate geometries between 2D and 3D and, as such, increase the reliability of method (i).

The paper continues as follows. Section 2 introduces the physical models, test programme and measurement systems. The SPH method and its implementation in DualSPHysics are briefly described in Section 3. The results in Section 4 include the calibration and validation of the numerical model, and provide new physical insight into the slide and wave kinematics, slide-water interaction power, wave energy and the effect of the water body geometry. In Section 5 the wave kinematics and wave heights are compared with existing theoretical models, and the implications of the results are discussed. The most relevant findings are finally summarised in Section 6.

2 Physical models

2.1 Overview

This section provides an overview of the physical model tests. The experimental data presented herein is based upon the laboratory set-up described in HS15, where further details may be found. The 2D experiments were conducted in the Coastal Wave Flume and the 3D tests in the Wave Basin, both located in the Hydrodynamics Laboratory of the Department of

Civil and Environmental Engineering at Imperial College London. The unobstructed area of the flume is 21.0 m (length) × 0.600 m (width), and the unobstructed area of the wave basin is 20.0 m (width) × 7.4 m (length). Fig. 1 shows a photograph of the set-up in the wave basin and Fig. 2 shows a schematic side view of the slide ramp and measurement systems. The ramp covered the entire channel width (2D) whilst its sides were extended by up to 7.75 m long walls in 3D. These walls were inclined at an angle of $\alpha = 45°$ corresponding to the ramp inclination (Fig. 1). Masses slid down on the PVC surface of the ramp purely driven by gravity. A stainless steel plate and a transition were fixed at the slope toe in both 2D and 3D. The transition was circular-shaped and formed an eighth of a circle of radius 0.60 m (Figs. 1 and 2).

2.2 Test programme and parameters

Two distinct 2D-3D test pairs are investigated herein, which are referred to as scenario 1 and scenario 2 (Table 1). Scenario 1 involves a rigid slide impacting into the 2D and 3D water bodies of depth h = 0.240 m resulting in a solitary-like wave in 2D (weakly-dispersive), whilst scenario 2 was conducted with a longer rigid slide with h = 0.480 m resulting in Stokes-like waves in 2D (strongly-dispersive). The tsunamis in both scenarios were generated by PVC slides, with the properties shown in the grey box in Fig. 2. Both slides were made of an identical front section, with different rear extensions, such that the identical force sensors, integrated in the front section, could be used. The relevant slide parameters, along with other experimental conditions, are shown in Table 1. The slide masses were m_s = 60.14 and 82.67 kg and the corresponding densities ρ_s = 1597 and 1451 kg/m^3. The slide widths b_s = 0.577 m and thicknesses s = 0.120 m were identical, whereas the lengths were l_s = 0.599 and 0.878 m (Fig. 2). The dynamic bed friction angles δ were theoretically derived with a kinetic and potential energy balance between slide release and impact location, including friction losses.

The slide impact velocity was measured (Section 2.3) such that the energy balance could be solved for the only unknown δ. Fig. 3 shows the shorter slide (scenario 1) on the slide ramp prior to release. The slide top surface was essentially flat as all fittings and electrical cables were integrated into the slide and the hooks to connect the slides to an overhead crane were removed prior to slide release.

Fig. 2 shows additional slide parameters namely the slide volume $\forall_s$, the slide front angle ϕ = 45° and the slide centroid impact velocity V_s. This velocity V_s is defined at the moment in time when the slide centroid reaches x = 0. Fig. 2 also illustrates the hill slope angle α = 45° and the still water depth h. In 2D the evolution of the wave parameters depends on the horizontal distance x, and in 3D on the radial distance r and the wave propagation angle γ. In both cases, the coordinate origin is placed at the intersection of the slide axis with the water surface and the hill slope face (Fig. 2). The origin of the coordinate along the hill slope x' is placed at the same location. The most crucial unknown wave parameters are the wave amplitude a, the wave height H and the wave period T.

Table 1 includes also the relevant dimensionless parameters, which can be derived with a dimensional analysis, as demonstrated by Heller et al. (2008). These include the slide Froude number $\mathsf{F} = V_s/(gh)^{1/2} \approx 1.51$ (scenario 1) and 1.17 (scenario 2) with gravitational acceleration g and relative slide thickness $S = s/h$ = 0.50 and 0.25. The relative slide mass is expressed as $M = m_s/(\rho_w b_s h^2)$ = 1.81 and 0.62 with the water (subscript w) density ρ_w.

2.3 Measurement system

The success of the present study relies on the accurate measurement of both slide and fluid properties. The unique combination of measurement systems includes (i) a cable-extension position transducer measuring the entire slide kinematics in both 2D and 3D, (ii) 15 force sensors integrated into the slide front to record the fluid pressures during the slide impact in

2D, (iii) particle image velocimetry (PIV) measuring the wave kinematics at various positions in 2D, (iv) resistance type wave probes recording the wave properties in both 2D and 3D and (v) a video camera for visual observations. Apart from the force sensors and the PIV system, the measurement systems were discussed in detail within HS15. The following paragraphs briefly outline the previously adopted measurement systems, but focuses on the detailed description of the two additional systems, (ii) and (iii) above.

The 15 force sensors (Honeywell - FSS1500NSB) were integrated into the slide front as shown in Figs. 2 and 3. They were arranged at different sections in the channel transverse direction in order to investigate pressure variation over the channel width and for redundancy. The distances of the sensors shown in Fig. 2 are provided relative to the slide edge before it was trimmed by 6 mm and rounded. The sensors were built into PVC strips in groups of five. The rear side of these strips hosted the electrical cables and the sensors were held in position with nylon screws. On the front face, the fluid pressed on T-shaped plugs with a head diameter of 12 mm, with the trunk guiding the force onto the sensor (see sketch at the bottom left corner of the box in Fig. 2). The entire strip was wrapped in a 0.3 mm thick rubber membrane to waterproof the transducers. The strips were then integrated into a slide front plate and fixed with silicon sealant. This plate was finally screwed onto the slide front part.

The linearity of the voltage-force relation of the herein analysed sensors was confirmed with precision weights with a coefficient of correlation $R^2 \geq 0.9999$. The risk to damage the sensors during an underwater calibration was reduced with a post-calibration based on the known submergence depths of each individual sensor for one particular moment in time. This calibration point was selected some seconds after slide impact for an interval where all the pressure signals, slide position and the free-water surface were reasonably stable, as confirmed by video recordings. Hydrostatic pressure was therefore assumed. This calibration procedure introduced an estimated measurement uncertainty of ±5% for the pressure data. The

sampling frequency was chosen between 8,333 Hz and 25,000 Hz, limited by the maximum capacity of the data acquisition system and the number of connected sensors. This relatively high frequency was selected to detect potential impulse pressures. However, as the slide front is oriented vertically during impact (hill slope angle + slide front angle $\alpha + \phi = 90°$), no impulsive pressures were observed such that a low-pass filter at 200 Hz was applied to the data to increase readability. Impulsive pressures may be expected for configurations with $\phi + \alpha > 90°$, where the slide front is inclined forward relative to the water surface, such that the front hits the water surface more violently.

The measurement locations of the wave probes are shown in Table 1. The wave properties were recorded at 128 Hz using resistance type wave probes located at relative distances $x/h = r/h$ = 3.0, 5.0, 7.5, 10.0, 15.0, 22.5 and 35.0 in both 2D and 3D, with some exceptions for wave run-up and for h = 0.480 m in 3D (Table 1). The wave propagation angles in 3D are γ = 0, 15, 30, 45, 58, 73 and 90° (onshore wave run-up). The onshore wave run-up probes consisted of stainless steel strips bonded to the surface of the side walls (Fig. 1). To maximise the effective basin area, and to minimise any associated wave reflections along the basin side-walls, the set-up in 3D was relocated and rotated for wave measurements in different directions γ (caption Fig. 1).

PIV was applied to measure the wave kinematics at several wave probe locations in the wave channel. To achieve this, the wave probes were removed, and the experimental test was repeated; the good repeatability of the laboratory set-up has been discussed in Heller and Spinneken (2013). A twin cavity Nd.YAG-laser light of 2 × 50 mJ energy and wave length of 532 nm at 15 Hz repetition rate (Litron Lasers) was used to illuminate the object plane. The laser cavity was located below the channel and the laser light was directed into the flume through the glass bottom resulting in the laser sheet shown in Fig. 2. A CCD camera with a resolution of 1,600 (height) × 1,186 (width) pixels was located approximately 1.2 m from the

flume glass wall and was oriented perpendicular to the light sheet. A wide angle lens was used resulting in an object area of 0.88 m (height) × 0.65 m (width). White seeding particles (Talisman 30) were used, and a black wall on the back side of the flume increased the visual contrast. The seeding was first mixed with water and then injected in the object plane. One illuminated seeding particle corresponded to 1-3 pixels on the raw image.

The images were recorded and analysed with the software Dynamic Studio (Dantec Dynamics). The double frame mode with a frame rate of 15 Hz was applied. A calibration plate was inserted into the object plane and used to derive the scale factor. Image distortion was neglected as only the vectors on the centre line of the image were analysed. A mean background subtraction was applied to the raw images in a pre-processing step. The velocity vector fields were determined using an adaptive PIV algorithm. The final interrogation area was 28 × 28 pixels corresponding to 15.5 mm × 15.5 mm. The post-processing included a moving average validation, which substituted spurious vectors with the average over neighbouring vectors (selected as 5 × 5 vectors), if they do not satisfy a particular acceptance factor (chosen as 0.12 herein). The vector results were then exported as .txt files for further analysis.

3 Numerical Model: smoothed particle hydrodynamics (SPH)

3.1 Theoretical background

This section provides a brief description of SPH, with further detail being available from reviews such as Monaghan (1992), Liu and Liu (2003), Gómez-Gesteira et al. (2010) and Crespo et al. (2015). SPH is a Lagrangian meshless method where the fluid is represented by nodal points or particles. Each nodal point represents a fluid particle with physical quantities f (mass m, density ρ, velocity vector $\mathbf{u}$, position vector $\mathbf{s}$, pressure p) interacting with neighbouring particles and moving according to the governing equations, in this case the

Navier-Stokes equations. Note that a common SPH notation is used herein, except that the subscript *p*, for particle, is added to some SPH symbols as they would otherwise conflict with the notation of the physical model tests. The values of the aforementioned quantities at a particular point are found by interpolation over the neighbouring particles (Dalrymple and Rogers, 2006; Gómez-Gesteira et al., 2010).

Only the final numerical expressions are shown herein as the full derivations are available elsewhere, e.g. in Gómez-Gesteira et al. (2010). Formally, the interpolation at a point **s** at time *t* for a particular quantity can be approximated in the continuous domain as

$$f(\mathbf{s},t) = \int_{\Omega} W(\mathbf{s}-\mathbf{x},h_p)\, f(\mathbf{x},\ t)\ \mathrm{d}\Omega, \qquad (1)$$

where **x** is the integration position, the integral is over the domain Ω and $W(\mathbf{s} - \mathbf{x}, h_p)$ is the weighting function or smoothing kernel. The kernel depends on the interpolation distance **s** – **x**, and the smoothing length h_p, which is a characteristic length used to determine the area of influence around **s**. A number of weighting functions are considered in the literature (Gómez-Gesteira et al., 2010); the function used for the present simulations is the cubic spline kernel (Section 3.2). For computational purposes, the continuous integral must be replaced with a discrete summation over particles *j* such that

$$f(\mathbf{s},t) \approx \sum_j \frac{m_j}{\rho_j} W\left(\mathbf{s}-\mathbf{x}_j,h_p\right) f_j, \qquad (2)$$

where the element of volume $\mathrm{d}\Omega$ has been replaced by m_j/ρ_j. Henceforth the value of the weighting function between particles *i* and *j* will be expressed as W_{ij}, referring to $\mathbf{s} = \mathbf{x}_i$, for brevity, where subscripts *i* and *j* denote the particles under consideration.

In the SPH method, the fluid flow is governed by the mass continuity and Navier-Stokes equations expressed in Lagrangian form as

$$\frac{1}{\rho}\frac{\mathrm{d}\rho}{\mathrm{d}t} = -\nabla \cdot \mathbf{u}, \tag{3}$$

$$\frac{\mathrm{d}\mathbf{u}}{\mathrm{d}t} = -\frac{1}{\rho}\nabla p + \nu_0 \nabla^2 \mathbf{u} + \mathbf{g}, \tag{4}$$

where **u** is the velocity vector, p is the pressure, ρ is the density, t is the time, ν_0 is the viscosity and **g** is the body forces. Herein, for the continuity equation the delta-SPH density diffusion formulation is used, first suggested by Molteni and Colagrossi (2009), as this has been shown to give noise-free pressure fields and close agreement with experimental data for wave propagation (Antuono et al., 2012; Altomare et al., 2015). Therefore, using the SPH divergence and gradient operators the conservation of mass for a particle is given by

$$\left(\frac{1}{\rho}\frac{\mathrm{d}\rho}{\mathrm{d}t}\right)_i = -\sum_j \frac{m_j}{\rho_j}\left(\mathbf{u}_j - \mathbf{u}_i\right) \nabla_i W_{ij} + \frac{2\delta_p h_p}{\rho_i}\sum_j m_j \bar{c}_{ijp}\left(\frac{\rho_i}{\rho_j} - 1\right)\frac{1}{r_{ijp}^2 + 0.01h_p^2} \nabla_i W_{ij}, \tag{5}$$

where δ_p is the delta parameter whose recommended value is 0.1, c_p is the speed of sound explained below, $\bar{c}_{ijp} = (c_{ip} + c_{jp})/2$ and r_{ijp} is the distance between particle i and j. Conservation of momentum is written in the form

$$\left(\frac{\mathrm{d}\mathbf{u}}{\mathrm{d}t}\right)_i = -\sum_j m_j \left(\frac{p_j}{\rho_j^2} + \frac{p_i}{\rho_i^2} + \Pi_{ij}\right)\nabla_i W_{ij} + \mathbf{g}, \tag{6}$$

where the additional viscous term Π_{ij} is added to Eq. (6) in order to represent viscous effects, to damp out flow instabilities resulting from particles moving chaotically, and to prevent particles from interpenetrating. A number of formulations have been proposed including the

artificial viscosity of Monaghan (1992) and the sub-particle scaling technique of Shao and Gotoh (2005) and Dalrymple and Rogers (2006); in the present simulation, artificial viscosity has been used (Section 3.2) as provided in DualSPHysics (Crespo et al., 2015).

The particle positions are updated using the XSPH correction of Monaghan (1989)

$$\left(\frac{\mathrm{d}\mathbf{x}_i}{\mathrm{d}t}\right) = \mathbf{u}_i + \epsilon \sum_j m_j \left(\frac{\mathbf{u}_i - \mathbf{u}_j}{\bar{\rho}_{ij}}\right) W_{ij}, \tag{7}$$

where $\varepsilon \approx 0.5$ and $\bar{\rho}_{ij} = (\rho_i + \rho_j)/2$. This correction prevents the problem of particle penetration by moving neighbours with approximately the same velocity.

The final equation needed relates the fluid pressure to density, using a relationship introduced into SPH by Monaghan (1994), namely

$$p = B\left[\left(\frac{\rho}{\rho_0}\right)^{\gamma_p} - 1\right], \tag{8}$$

where $\gamma_p = 7$, $\rho_0 = 1000$ kg/m^3 is the reference density and the value of B determines the reference speed of sound c_{0p}. Theoretically, the speed of sound c_p depends on the derivative of pressure with respect to density,

$$c_p^2(\rho) = \frac{\partial p}{\partial \rho} = \frac{B\gamma_p}{\rho_0}\left(\frac{\rho}{\rho_0}\right)^{\gamma_p - 1} \tag{9}$$

such that $B = {c_{0p}}^2\rho_0/\gamma_p$, where c_{0p} is the speed of sound at the reference density ρ_0. It has been noted, however, that using the weakly compressible SPH formulation of Eqn. (3) and (4), realistic speeds of sound are hard to achieve in SPH as the time step resulting from the CFL criterion is too small (Gómez-Gesteira et al., 2010); therefore, the value of c_p is usually taken

as ten times higher than the maximum wave velocity to be measured (Dalrymple and Rogers, 2006; Gómez-Gesteira et al., 2010).

The implementation of boundary conditions (BCs) has proven problematic in SPH as the particle summation of Eq. (2) must be undertaken without any interaction with the area outside the boundary (Crespo et al., 2007). In general, four implementations of BCs are possible: (a) dynamic, in which the boundaries are represented by fluid particles that satisfy the same equations as the fluid but are fixed in place, or are images created at runtime, or are moved with a prescribed function, (b) repulsive, in which a fluid particle experiences a greater force according to a prescribed function as it approaches a boundary, (c) semi-analytical where the missing kernel support is included analytically (Mayrhofer et al., 2013) and (d) periodic, in which particles near a boundary interact with particles on the opposite side of the domain, across a complementary open boundary (Gómez-Gesteira et al., 2010). The BCs adopted herein are the dynamic BCs as these are the only BC present in DualSPHysics (Section 3.2).

With the above framework in place, the equations may be solved using a time stepping technique. Numerous algorithms are available for this purpose, with the Verlet algorithm used in the present study (Section 3.2).

3.2 Implementation in DualSPHysics and performance

The SPH open source code DualSPHysics with the beta executable of v3.1 was used herein (Crespo et al., 2011, 2015; Canelas et al., 2013); the DualSPHysics code is derived from an earlier implementation of the SPH method called SPHysics, which has previously been harnessed for landslide-tsunami investigations. In the following description, the code options selected for the purpose of the present work are shown in italic. DualSPHysics v3.1 offers various time integration schemes (*Verlet*, symplectic), kernel functions (*cubic spline*, quintic

Wendland), density filters (Shepard, *Delta-SPH formulation*), viscosity treatments (*artificial*, laminar + sub-particle scale turbulence model) and BCs (*dynamic*, periodic open). Initial tsunami simulations were conducted with the numerical parameters and coefficients adopted from the dam break test case (Crespo et al., 2015), with parameters subsequently optimised for closest agreement between the numerically and experimentally deduced wave amplitudes. Some experience for this optimisation was gained from parameter variations in SPHysics and an available landslide-tsunami test case in the SPHysics user software. The numerical runs presented herein were conducted on the Imperial College London HPC CX1 cluster (the herein accessed section involved 12 core Westmere nodes Intel® Xeon® CPU X5650 at 2.67 GHz with DDR3 memory running at 1333 MHz), with the formulations, numerical parameters and constants show in Table 2.

The beta executable v3.1 includes a discrete element method (DEM) formulation such that solid-solid and solid-fluid interactions may be simulated. For the purpose of these interactions, the inter-particle forces of rigid body particles are derived from contact law theories. The DEM particles are regarded by the fluid particles as SPH particles, allowing for a natural coupling between SPH and DEM (Canelas et al., 2013). These features are essential for the present work as the slide is modelled as a floating object moving along a rigid-ramp boundary. The DEM formulation is based on a Young's modulus, Poisson ratio, mass and a bed friction coefficient, with all relevant values being shown in Table 2. The Young's modulus and the bed friction coefficient were varied in a sensitivity analysis resulting in no noticeable effect on the tsunami generation. This may be due to individual particles trapped between the slide and boundaries lubricating the contact areas, as well as the accumulation of vibration energy between the surfaces reducing the contact friction (personal communication, Ricardo Canelas, Portugal). The corresponding challenges are currently being addressed by the DualSPHysics developers.

Post-processing tools BoundaryVTK and MeasureTool are included within DualSPHysics. These tools were used both to visualise the results and to extract the kinematics and the free surface data at a set of points. The free surface is visualised as a mass isosurface, taken at a threshold mass value of 0.5 herein. The numerical values, e.g. the location of the free surface, were computed by means of an SPH interpolation (Wendland kernel, in contrast to the cubic spline kernel used during the simulation) of the values of the neighbouring particles around a given position.

For simulations of this type, it is instructive to illustrate the computational runtimes. All simulations were performed on 12 CPUs with the formulations given in Table 2. The initial distance between particles was dp = 10 mm, except for a number of convergence tests, which also considered dp = 7.5 and 15 mm. The shortest simulation (2D, numerically treated as a three-dimensional problem herein, h = 0.240 m, 15 mm initial distance between particles dp) took 14 min per second of real time and involved 318,347 particles. The computationally most expensive simulation (3D, h = 0.480 m, dp = 10 mm) took 60 h per second of real time and included 23 million particles. Problems involving more than 1000 million particles for free-surface flows have been already investigated with DualSPHysics using the multi-GPU version (Domínguez et al., 2013; Valdez-Balderas et al., 2013). Nevertheless, Section 4.2 including a convergence study and Section 4.3 show that dp = 10 mm provides a good compromise between simulation time and accuracy for the present purpose based on the CPU version.

4 Results

4.1 Physical model results

This section investigates two selected 2D-3D test pairs from HS15 in detail relying on novel, unpublished results. The 2D and 3D tests were conducted under identical BCs (slide, slide

impact velocity), and only differ in the type of the water body geometry. Two distinct test pairs were selected, namely one involving a solitary-like wave (weakly-dispersive, scenario 1) and one involving Stokes-like waves (strongly-dispersive, scenario 2) in 2D.

Fig. 4 shows series of images of scenario 1 in 3D with a time interval in Fig. 4b onwards of 0.2 s. The slide is in its release position in Fig. 4a and impacts into the water body in Fig. 4b generating an impact crater which further increases and reaches the wave probes at r/h = 3 in Fig. 4c. This crater is largest along the slide axis and the onshore wave run-up at γ = 90° is considerably smaller. Most slide energy is transferred within the first 0.50 s (Section 4.1.2) such that the most crucial part of tsunami generation is already concluded in Fig. 4d. The crater trim collapses in Fig. 4d, and a highly non-linear water surface elevation is being created with an up-rush in the wake of the slide. Fig. 4e shows the typical semi-circle of primary wave propagation in 3D. The immediate slide impact area is characterised by air detrainment and a high degree of turbulence. The semi-circle of the primary wave increases in Fig. 4f followed by the smaller secondary wave, which is generated by the run-down of the previous up-rush.

4.1.1 Slide positions and kinematics

Fig. 5 shows the slide positions of both scenarios in 2D (black lines) and 3D (grey lines) measured with the position transducer. At time t = 0 the slide nose reaches the still water surface (x' = 0). The position measurement follows x' as long as the slide moves parallel to the ramp, i.e. until the slide nose reaches the transition. For any subsequent times, the measured distance between the slide rear and the position sensor deviate from the x' coordinate. The tests in 3D were repeated under small variation of the slide release position until the slide centroid impact velocity $V_{s,3D} = V_{s,2D}$ ±5% for two corresponding tests. As a result, the slide release positions in 2D (subscript 2D) and 3D (subscript 3D) differ slightly in Fig. 5a with x' =

–0.55 m (2D) and –0.47 for (3D, Table 1), whilst they are identical in Fig. 5b for both geometries in scenario 2.

In both scenarios the slides in 3D run-out farther than in 2D, particularly for scenario 2 in Fig. 5b. This is likely to be due to a small sub-pressure occurring below the slide when it passes over the transition. This is a direct consequence of the slide lengths, which are sufficiently long such that the slides are only supported at two contact points over the transition. This sub-pressure effect is believed to be larger in 2D, with limited lateral water supply when compared to 3D. The radius of the transition (0.60 m) was selected to be relatively large in order to limit this sub-pressure effect. Fortunately, if physical and numerical model results are considered individually, this effect is only expected to have a minor influence on the present results. This is because the main wave generation process is already concluded once the slide reaches the transition (Section 4.1.2). However, this effect may play an important role if physical and numerical results are compared with one another, as the numerical model is currently not able to take this effect into account. This point will be discussed in more detail in Section 4.2.

Fig. 5 also includes the slide velocities, which were directly derived from the positions through numerical differentiation. The slide reaches its peak velocity shortly after its nose reaches the still water surface. The slide centroid impact velocities V_s, marked with arrows in Fig. 5, are smaller than the peak velocities for both scenarios, namely $V_{s,2D}$ = 2.32 m/s in Fig. 5a and $V_{s,2D}$ = 2.53 m/s in Fig. 5b. In the context of the numerical simulations, particularly relevant is the slide front (subscript f) impact velocity V_{sf}. The velocity V_{sf} is similar in magnitude to the slide centroid impact velocity V_s in scenario 1, but V_{sf} is considerably smaller than V_s in scenario 2 (Fig. 5b). This is believed to be due to the larger dominance of the gravity force on the slide in scenario 2, which is at the initial phase of slide impact still considerably larger than the opposing friction, drag and buoyancy forces. As a result, the

longer slide in scenario 2 is longer accelerating in this initial phase than the shorter slide in scenario 1, resulting in $V_s > V_{sf}$ for scenario 2. Fig. 5 also illustrates the simulated slide positions and velocities, which will be discussed in Section 4.2.

4.1.2 Instantaneous pressures and power in 2D

The analysis of the pressure data showed that for one particular height on the slide front (e.g. for S1, S6, S11), all three sensor signals are practically identical. The pressure distribution is thus uniform across the slide width, and boundary or side gap effects are insignificant, at least up to 14.5 mm from the slide edge (Fig. 2). Fig. 5c,d shows the measured pressures in one section involving sensors S1, S3, S4 and S5 versus time for scenario 1 (Fig. 5c) and scenario 2 (Fig. 5d). The pressure at S1, most adjacent to the slide nose, increases first, followed by similarly shaped signals measured by S3, S4 and S5. The peak pressure at S1 in scenario 1 is 5,713 Pa, and this value is 2.4 times larger than the hydrostatic still water pressure at the channel bottom ($\rho_w gh$ = 2,353 Pa). The corresponding peak of 5,561 Pa in scenario 2 is similar in magnitude. The peak's maximum is mainly dominated by the slide front impact velocity V_{sf}, which is similarly large for both scenarios (Table 1). However, the peak value of 5,561 Pa in scenario 2 only corresponds to a factor of 1.2 times the hydrostatic still water pressure at the channel bottom (4,707 Pa). This is considerably smaller than in scenario 1, and indicates that the larger water depth is of limited relevance for the pressure formation at this initial stage. The pressure signals of the remaining sensors S3, S4 and S5 in both scenarios are delayed compared to S1 and of considerably smaller magnitude; the pressure peak at S5 at the corresponding time as for sensor S1 is approximately 4.5 times smaller in scenario 1 (Fig. 5c) and 3 times smaller in scenario 2 (Fig. 5d). The second peak at $t \approx 0.4$ s may be caused by the backflow, which eventually results in the up-rush in the slide wake (Fig. 4e). The magnitude of the initial peaks at S5 are exceeded at t = 3 s. This is particularly distinct for scenario 2

with a larger water depth (Fig. 5d). Note that the entire slide in scenario 1 reaches the channel bottom at about t = 1 s whilst in scenario 2 only the slide front reaches the bottom with the slide rear still remaining on the ramp at t = 3 s.

Fig. 5c,d also includes the hydrostatic pressure (dashed lines) derived at the height of each individual force sensor when the slide sits (or would sit) flat on the channel bottom. Deviations between the hydrostatic pressure and the pressure signals at t = 3 s are expected, as the free water surface is unsteady at this stage and the sensors measure a combination of static and dynamic pressure components, and the slide does not sit flat on the bottom in scenario 2.

The final parts of Fig. 5 illustrate the instantaneous slide-water interaction power $P(t)$ deduced at the slide front surface. As the slide front is the main interface to transfer energy between slide and water, $P(t)$ may give a good indication when and how much slide energy is transferred to wave energy. The power was computed through

$$P(t) = F(t)V(t)\cos\alpha, \tag{10}$$

where the instantaneous force $F(t)$ on the slide front was computed from the spatial integration of the pressure signals in Fig. 5c,d. For this integration, the unknown boundary values were approximated with the values from S1 (nose) and S5 (top) and the resulting 6 points were interpolated using a cubic spline over the slide front as shown in the insets in Fig. 5e,f. The insets correspond to selected moments in time, and include the pressure distribution prior to the power peak, at the peak, and post-peak at t = 1.0 s. The pressure magnitudes in these distributions increase with time starting from the slide nose, reach their maxima at the power peak and result then in a nearly linear distribution at t = 1.0 s, when both slide noses reached the channel bottom. These pressure curves, integrated over the slide height and

multiplied by the slide width, resulted in $F(t)$. The instantaneous velocity $V(t)$ is available from Fig. 5a,b.

Fig. 5e,f shows that the major slide power peaks of 417 and 454 W occur at about 0.2 s in both scenarios. Nearly all energy is transferred within 0.5 s. Video recordings and Fig. 4 confirm that this closely relates to the time interval in which an impact crater forms, and where the most important tsunami generation phase takes place. For such fast impacting slides (V_{sf} = 1.67 - 2.43 m/s), the front face is mostly responsible for the tsunami generation process. This explains why the relative slide volume M typically only has a secondary effect on the wave magnitude; the primary drivers being the slide Froude number F and the relative slide thickness S.

4.1.3 Tsunami wave propagation

Fig. 6a-d shows the relative water surface elevations η/h of the 2D test of scenario 1. The abscissa shows the dimensionless time $t(g/h)^{1/2}$, and the water surface elevations are shown for different wave probe locations along the slide axis (γ = 0). Fig. 6e-h includes the corresponding data of the 3D test, with the associated still images being shown in Fig. 4. Note that the scale on the ordinate in the 3D case is increased by a factor of 2, 3 and 9 in Fig. 6f,g,h, respectively.

The 2D relative primary wave amplitude at the first wave probe is a_{2D}/h = 0.189/0.240 = 0.79 and the corresponding 3D amplitude is only approximately 30% smaller with a_{3D}/h = 0.136/0.240 = 0.57. However, the 3D wave decays considerably faster than the 2D wave. In Fig. 6d,h the primary wave amplitudes reduce to a_{2D}/h = 0.156/0.240 = 0.65 and a_{3D}/h = 0.010/0.240 = 0.04, respectively, resulting in a difference of a factor of 16. Similar trends are observed in Fig. 7, showing the water surface elevation for the test pair of scenario 2. For scenario 2 the relative primary wave amplitude at the first wave probe is a_{2D}/h = 0.110/0.480

= 0.23 (Fig. 7a) and the corresponding 3D amplitude is a_{3D}/h = 0.037/0.480 = 0.08 (Fig. 7e). As a result, the 2D and 3D tests differ by a factor of 3 in the slide impact zone; this being in marked contrast to the only 30% deviation observed in scenario 1. At $x/h = r/h$ = 22.5 the values are a_{2D}/h = 0.056/0.480 = 0.12 (Fig. 7d) and a_{3D}/h = 0.004/0.480 = 0.01 (Fig. 7h). This again results in a difference of a factor of 16. The waves in scenario 2 can be categorised as Stokes-like waves (Heller and Hager, 2011) and are thus more dispersive than the solitary-like wave in 2D in scenario 1. Figs. 6 and 7 clearly illustrate the relevance of the effect of the water body geometry, and the associated need to investigate intermediate geometries.

4.1.4 Wave kinematics and energy in 2D

Figs. 8 (scenario 1) and 9 (scenario 2) show the water particle velocity vector fields over one wave period T at different wave probe locations. Each velocity vector represents the average velocity within an area of 15.5 mm × 15.5 mm, and the velocity values are given in 1/15 s intervals (Section 2.3). The reference vector in the top right corner of each subplot represents the linear shallow-water wave speed $(gh)^{1/2}$, namely 1.53 m/s in Fig. 8 and 2.17 m/s in Fig. 9. The particle velocities start from zero and increase to their maxima below the crest. These maxima are on the order of 80-90% of $(gh)^{1/2}$ for the solitary-like wave (Fig. 8) and about 20% of $(gh)^{1/2}$ for the Stokes-like wave (Fig. 9). A reverse flow can be observed in the wave trough which is, relative to the velocities below the crest, more distinct for the Stokes-like wave. Velocity vectors are unavailable in the proximity of the channel bottom in Fig. 9. Fortunately, the velocity distribution in Fig. 9 is relatively uniform over depth. For the following energy calculations, this region was populated, at each time step, with the mean velocity vectors of the two deepest recorded vectors.

The kinetic (subscript kin) ΔE_{kin} and potential (subscript pot) ΔE_{pot} wave energies for each time step Δt were extracted from Figs. 8 and 9 as

$$\Delta E_{kin} = \left(\frac{1}{2}\right) b\rho_w \Delta t c \int_{-h}^{\eta} \left(v_{px}^2 + v_{pz}^2\right) \mathrm{d}z \quad (11)$$

$$\Delta E_{pot} = \left(\frac{1}{2}\right) b\rho_w g \Delta t c \eta^2 \quad (12)$$

In Eq. (11) v_{px} and v_{pz} are the particle velocity components in the x (subscript x) and z (subscript z) direction, respectively. The time step Δt is taken as either the PIV or wave probe sampling interval, namely 1/15 s for Eq. (11) and 1/128 s for Eq. (12). The main simplification in Eqn. (11) and (12) is that each section of the wave travels with the (crest) wave celerity c, whereas in reality the crest and trough may propagate with a different wave speed (Fritz et al., 2004). This simplification may cause an estimated error of 10%.

The total kinetic E_{kin} and potential E_{pot} wave energies can be estimated with

$$E_{kin} = \sum_T \Delta E_{kin} \quad (13)$$

$$E_{pot} = \sum_T \Delta E_{pot} \quad (14)$$

The energy values are shown in Table 3. To date, only a very limited number of studies (e.g. Heller, 2007) measured the kinetic energy in landslide-tsunamis. In most other studies (e.g. Kamphuis and Bowering, 1972; Mohammed and Fritz, 2012), the potential wave energy was deduced from wave profile measurements and equipartition of kinetic and potential wave energies was assumed, according to linear wave theory. However, landslide-tsunamis are commonly highly non-linear, and this is reflected by the differences in kinetic and potential wave energies in Table 3.

For the solitary-like wave in scenario 1, the kinetic wave energy is 6-30% larger than the potential energy. Solitary wave theory indeed predicts that the kinetic energy is larger than potential energy (Li and Raichlen, 2003). The tsunami in scenario 1 contains (76/161.8)·100 = 47% of the kinetic slide energy computed with V_s and the remaining 53% are included in the

trailing waves or dissipated. The Stokes-like wave in scenario 2 is less non-linear and the kinetic and potential energies are identical large, at least at x/h = 5.0. The primary wave includes (48/264.7)·100 = 18% of the maximum kinetic wave energy. A substantial part of the energy in scenario 2 may be transformed to the trailing waves. Note that the total wave energy of the primary wave with propagation distance is approximately conserved in both scenarios.

Table 3 also includes the energies transferred from the slide front to the water body, as found by integrating the power curves in Fig. 5e,f over time. The value of 123.3 J in scenario 1 is (123.3/468.5 – 1)·100 = – 74% smaller than the physically possible upper limit given by $m_s g\Delta z$ = 468.5 J, with Δz = 0.795 m as the height difference between slide centroid release and deposit positions. In scenario 2, the value 112.6 J is (112.6/747.4 – 1)·100 = – 85% smaller than $m_s g\Delta z$ = 747.4 J, with Δz = 0.922 m. The slide is considerably less efficient in scenario 2 for tsunami generation. The wave energies measured in the primary waves are with (76/123.3)·100 = 62% and (48/112.6)·100 = 43% smaller than the energies transferred by the slide front. This is consistent with video recordings showing that the slide front creates an impact crater collapsing on top of the slide. This creates a forward flow, resulting in the primary wave, and a backward flow, which does not contribute to the primary wave.

4.2 Calibration and validation of DualSPHysics

4.2.1 Overview and wave profiles

The numerical model tests in DualSPHysics were calibrated with the physical model tests conducted in 2D (treated as a three-dimensional problem) and validated with the 3D tests. Fig. 10 shows the seven numerical domains of scenario 1. This includes both a side view and a plan view of the 2D geometry (Fig. 10a,b) and plan views of the remaining six geometries (Fig. 10c-h). The overall domain length from the rear of the ramp to the end of the water body is 4.96 m in all cases. The ramp is 0.90 m long such that the pure water body length is 4.30 m

(4.96 – ramp length + h) corresponding to $x = 7.5h + 2.50$ m. As a result, reflections are avoided for the primary wave at $x/h = 7.5$. The overall 3D domain is 6.45 m wide, which is composed of 4.30 m to the right hand side, where the measurements were taken, and 4.30/2 m to the left hand side. Very similar geometric configurations are applied to scenario 2, except that the ramp length is 1.14 m and that the overall domain length is 6.76 m in 2D with a water body length of 6.10 m. This once again corresponds to $x = 7.5h + 2.50$ m with $h = 0.48$ m. The remaining geometries in scenario 2 were slightly shorter, yet sufficiently long to avoid reflections of the primary wave at $x = 7.5h$.

The slides were modelled as floating objects (Section 3.2). In the interest of computational time, the slide started with the nose at the water surface with an initial slide front impact velocity V_{sf}. To release the slide further up the ramp would have resulted in approximately 15% additional, but unnecessary, computational effort because in the interval between the slide release and the nose impact on the water surface the water would have remained undisturbed. Additional computational resources were also saved with this strategy, as the numerical ramp length and thus the number of boundary particles was reduced.

The velocities V_{sf} were initially selected as the measured values from the physical model tests (Fig. 5a,b). However, this resulted in numerically generated wave amplitudes in excess of the physical model tests and even wave breaking in scenario 1. To enable a direct comparison between the numerical and physical tests, the initial numerical slide velocity was reduced until a reasonable agreement in terms of wave amplitudes was achieved. The slide velocities measured in the physical model tests and the final selected numerical values are shown in Table 4. The numerical values were reduced by approximately 50% to achieve a good agreement between the physical and numerical wave amplitudes. Fig. 11a,b shows the experimental and numerical wave profiles of scenario 1 with and without reduced numerical slide impact velocity. The waves would have been considerably overestimated without a

reduction in slide velocity, resulting in wave breaking and, as a result, a too large wave decay. The slide kinematics of the numerical and physical model tests is discussed in more detail in Section 4.2.2. It is important to stress that the slide volume, mass, density and geometry, the water depth, the slope transition as well as the water body geometries were identical between the numerical and physical model tests.

Fig. 12 shows the numerical simulation of the test corresponding to the experimental observations in Fig. 4. The slide is released in Fig. 12a from its initial position with an initial velocity. It then impacts into the 3D water body in Fig. 12b and generates a splash which is considerably smaller than in the physical model test (Fig. 4b). This marked difference is due to the initial distance between particles of 10 mm, for which the water sheet or individual droplets cannot adequately be simulated. This clearly results in some deviations in the slide impact zone between Figs. 12 and 4. Despite these differences, the important features, namely the overall shape of the primary wave including its propagation on a semi-circle and the spatial variation in amplitude from the main impulse direction ($\gamma = 0$) towards the peripheries, are simulated qualitatively correctly.

The numerically deduced wave profiles are compared with the measured profiles in Figs. 6 (and the zoomed in version in Fig. 11) and 7, resulting in small deviations within 11% relative to the primary wave amplitude a in 2D. The agreement is particularly good in Fig. 7b, with only 4.8% deviation in a. After this successful calibration in 2D, both scenarios are validated against the 3D tests (Figs. 6e,f, 7e,f and 11c,d). In this context, it is important to highlight that slide impact velocities remained those calibrated for the 2D cases (Table 4). In the 3D comparisons, the maximum deviations between the physical and numerical amplitudes a of the primary waves are –20% (Fig. 7f) and +33% (Fig. 11c). The best overall agreement in 3D is achieved in Fig. 11d with a deviation of –8%. In considering Figs. 6, 7 and 11, the

numerical prediction of the trough length and the secondary wave are particularly challenging; the underlying reasons being discussed in Section 4.2.2.

4.2.2 Slide kinematics and further reasons for discrepancies

The primary reason for discrepancies between numerical and experimental tests may be the differences in slide kinematics. The numerical slide positions and velocities are shown in Fig. 5a,b as dashed lines. The latter are derived from the position through numerical differentiation and then approximated with a 2nd order Fourier series representing the data with a coefficient of determination of $R^2 \geq 0.94$. A sub-pressure may build below the slide in the physical model tests as the slide passes the transition (Section 4.1.1), and this effect can currently not be represented in DualSPHysics v3.1. This sub-pressure decelerates the physical slide. Furthermore, the modelling of the friction between the slide and ramp surface is challenging (Section 3.2). The combination of the sub-pressure effect and the friction are likely to be the main reasons why the numerical slide impact velocity had to be reduced in order to match the wave amplitudes of the physical model tests (Figs. 6, 7 and 11).

Besides the slide kinematics, the initial distance between particles of 10 mm may be an additional source of discrepancies between numerical and physical model results, as the numerical water particles are unable to penetrate into areas such as the side gaps between slide and channel walls. This may result in higher energy transformation to the tsunami. A convergence study of the water surface elevation in 2D has been conducted to show the dependence on the initial distance between particles. Fig. 13 shows the comparison of three SPH simulations with the physical model data for the water elevation of the solitary-like wave of scenario 1 at three relative distances x/h. The agreement with the physical model data is satisfactory for the SPH model described in Section 3. With decreasing particle size, there is a general convergence for x/h = 5.0 and 7.5. For x/h = 3.0, the agreement is satisfactory even if

the convergence is unclear, which is mainly due to the proximity to the slide impact zone where non-linearities and multi-phase effects might have greater influence. These results are in agreement with similar studies using DualSPHysics (Cunningham et al., 2014; St-Germain et al., 2014).

Finally, it is very encouraging to observe that DualSPHysics v3.1 accounts for the slide-water-sidewalls interaction in the sense that the slide kinematics between 2D and 3D differ, despite the fact that the slide impact velocities and friction factors remain constant. Such differences are also observed in the physical model tests.

4.2.3 Wave kinematics

The numerical and experimental wave kinematics in the crest regions are compared in a final step of this calibration and validation procedure. This comparison is linked with a more detailed analysis of the water surface elevations, particularly in the vicinity of the maximum crest. Fig. 14 illustrates the PIV measurements on the upper subplots and the numerical simulations on the lower subplots. The velocity vectors are shown over t'/T, with the wave period T and the shifted time t', such that $t' = 0$ corresponds to the maximum crest elevation. For scenario 1 the wave crests are considered at $x/h = 7.5$, with $x/h = 5.0$ for scenario 2. The numerical wave profiles tend to be slightly steeper than the measured profiles. The agreement between the experimental and the numerical velocity vectors is very good for scenario 1 (Fig. 14a,b). For scenario 2 (Fig. 14c,d), however, the numerical values systematically overestimate the velocity vectors. The reason for this discrepancy may again be due to the differences in experimental and numerical slide kinematics (Fig. 5b).

It may be concluded that SPH works well for violent impacts resulting in one dominant primary wave such as in scenario 1, and slightly less well for less energetic Stokes-like waves. This may particularly be apparent some distance away from the source where the trailing

waves (which are not well modelled in scenario 2) may transfer their energy to the primary wave via frequency dispersion. The possible numerical sources for the less close agreement between numerical and experimental results in scenario 2 in relation to scenario 1, and for numerical and experimental disagreements in general, may be numerous including using a weakly compressible SPH formulation (as opposed to a strictly incompressible SPH scheme), use of single precision in the computations within DualSPHysics v3.1, numerical dissipation in the time integration scheme, the effect of the boundary condition in retarding the flow, the choice of SPH smoothing kernel, the role of the artificial viscosity for a given particle size etc. All these sources are currently under investigation within the SPH community (see SPHERIC Grand Challenges: http://spheric-sph.org/grand-challenges). Nevertheless, taken as a whole, the agreement between numerical and physical model tests in Figs. 6, 7 and 11 looks promising, such that in the following Section 4.3 wave propagation in intermediate geometries is investigated purely numerically.

4.3 Numerically investigated intermediate geometries

This section addresses wave parameters from five intermediate water body geometries between 2D and 3D including the 3Dc case (Fig. 10). Fig. 15 shows the relative wave amplitude a/h along the slide axis for all seven geometries. The data are illustrated as a function of the relative distance, x/h or r/h, for both scenario 1 (Fig. 15a) and scenario 2 (Fig. 15b). Considering scenario 1 first, the relative wave amplitudes for the various geometries at $x/h = r/h = 3.0$ are similar in magnitude, and lie at $a/h = 0.73 \pm 10\%$. In contrast, a factor of 2.9 between the 2D and the 3D amplitudes are observed at the same location for scenario 2.

The wave amplitudes for a geometry with a channel side wall angle of $\theta = 7.5°$ are approximately halfway between the values observed in 2D and 3D, and the 3D wave amplitudes are approached very rapidly with increasing θ. For $\theta = 30°$ (scenario 1) and $\theta =$

45° (scenario 2), the observed wave amplitudes are practically identical to those in 3D. As a result, the 3D case may be investigated in a geometry with $\theta = 45°$ for cases where only the maximum amplitude along the slide axis is of interest. This finding is useful to save 25% of the computational cost for numerical simulations, or laboratory space in a physical model. The 3Dc geometries clearly differ from the 3D cases as evident in Fig. 15; the relative wave amplitudes a/h being close to the values for $\theta = 7.5°$ in scenario 1, and lying between the values for $\theta = 15$ and 30° for scenario 2. Tsunamis in 3Dc are therefore clearly smaller than in 2D, yet substantially larger than in 3D.

Fig. 16 shows the relative wave heights H/h at the same locations and for the identical geometries as in Fig. 15. Similar features as previously described for the amplitude are observed in Fig. 16, namely that the wave heights approach the values in 3D relatively rapidly with increasing θ, and that the values measured in 3Dc differ substantially from both 2D and 3D.

The wave period T in the numerical tests is not considered further, as Heller et al. (2012) showed that T does not change significantly with the water body geometry. This was also confirmed by HS15, establishing that T changes considerably less with the water body geometry than the amplitude or height. It is critical to stress that the findings in Figs. 15 and 16 support landslide-tsunami hazard assessment method (i) in Section 1.1.2, as the wave parameters in additional water body geometries between 2D and 3D can now be estimated. To date, generic empirical equations were limited to 2D and 3D geometries.

5 Discussion of results

5.1 Comparison of fluid kinematics with theoretical formulations

The accurate description of wave kinematics is important for a number of applications, such as evaluating the kinetic wave energy, calibrating and validating the coupling of SPH with a

computationally less expensive wave propagation model (Narayanaswamy et al., 2010; Abadie et al., 2012) or to investigate fluid loading on structures. The measured kinematics are compared with a set of non-linear, non-hydrostatic wave theories, aiming to predict theoretically the kinematics through a set of given wave parameters. A wide range of analytical and semi-analytical wave theories exist. However, these are often restricted to specific ranges of validity, most commonly due to their assumption concerning the relative water depth and/or the relative wave steepness. The theories considered herein are a 5^{th} order Stokes solution (Fenton, 1985), a 2^{nd} order Cnoidal model (Wiegel, 1960), a higher order solitary wave theory (Munk, 1949) as well as stream function theory (Dean, 1965).

Non-linear Stokes based expansions describe a periodic wave with a steeper crest and a flatter trough than predicted by linear wave theory. The formulation of the velocity potential involves a series expansion in terms of the wave steepness H/L, with L as the wave length, which has been undertaken analytically up to the 5^{th} order (Fenton, 1985). Stokes-like expansions are expected to work best for an Ursell parameter $U = HL^2/h^3 < 10$ (Keulegan, 1950), and are often considered unsuitable for very shallow water. In contrast, cnoidal wave theory allows periodic waves to exist in shallow water, and its profile is described by the Jacobi elliptic function "cn". Cnoidal wave theory is bridging the range between linear wave theory and solitary wave theory (for $T \rightarrow \infty$) and is considered most appropriate for $U > 25$. Solitary wave theory is often used to model tsunamis, particularly due to seismic sources. It consists of a non-periodic wave crest elevation, with no wave trough, and its wave length is theoretically infinite such that $U \rightarrow \infty$. This shallow-water wave involves considerable fluid mass transport, and its shape remains constant along a prismatic wave channel, as non-linearity and dispersion are in balance and viscous effects are excluded (Munk, 1949). Stream function theory describes a method to evaluate the water particle kinematics based upon a given surface profile or, as applied herein, by the given wave parameters height, period and

water depth. The stream function solution is found iteratively as a solution of Laplace's equation, satisfying (numerically) the bottom BC as well as the kinematic and dynamic free-surface conditions. The fluid kinematics are then computed as the derivatives of the scalar stream function (Dean, 1965).

Fig. 17 shows the fit of the above theoretical wave formulations to the measured wave profile for both scenario 1 (x/h = 7.5, Fig. 17a) and scenario 2 (x/h = 5.0, Fig. 17b). The wave profiles were time shifted such that t' = 0 corresponds to the maximum crest elevation; all profiles being shown over one wave period T. The analytical expressions required to compute the wave profiles and water particle kinematics are excluded here for brevity, and reference is made to Fenton (1985) (5^{th} order Stokes), Wiegel (1960) (2^{nd} order cnoidal), Munk (1949) (higher order solitary) and Dean (1965) (stream function). The evaluation of the theoretical wave profiles is based upon the experimental amplitudes and up-crossing periods. Note that the theories reach, and sometimes even exceed, their limit of applicability. This is particularly important in the context of scenario 1, where the wave propagates in very shallow water (h = 0.24 m, Table 1). To facilitate a consistent comparison to the aforementioned theoretical formulations, only the wave theories that converged for the particular water depth of a scenario are shown. In scenario 1, this is limited to the higher order solitary solution, whilst all four formulations (2^{nd} order cnoidal, higher order solitary, 5^{th} order Stokes and stream function) are applicable to scenario 2 (Fig. 17).

In Fig. 18 the wave kinematics below the crest are compared for both scenario 1 (Fig. 18a) and 2 (Fig. 18b); all parameters being identical to those described in the context of Fig. 17. Note that the PIV vectors were not smoothed to keep them as realistic as possible. Furthermore, the numerical values essentially confirm what was already discussed in Section 4.2.3, namely that they match the wave kinematics well for scenario 1 and over-predict the measured values of scenario 2. The higher order solitary wave theory represents the measured

profile in Fig. 18a very well. For scenario 2 (Fig. 18b) all four wave theories are in reasonably good agreement with the experimental data. In an average sense, the higher order solitary wave theory provides a good description. However, this theory fails to match the surface elevation (Fig. 17b). Taken as a whole, 5th order Stokes theory and the stream function solution are considered most suitable. Indeed, their prediction is very similar, which is unsurprising given the wave parameters of scenario 2.

Table 5 shows a quantitative comparison of the wave kinematics derived from the analytical theories, PIV measurements and SPH simulations. The comparison includes two measures: the maximum and the mean horizontal water particle velocities in the crest region. The mean horizontal velocities were computed as the mean between the still water level SWL and the maximum crest elevation. The numerical (SPH) values are also included, essentially confirming previous findings (Section 4.2.3); the discrepancy between the mean numerical and experimental values in scenario 1 being (1.12/0.97)·100 = 15%. The mean velocity of 0.97 m/s is represented very well by the solitary wave theory with 0.99 m/s (+2%). The solitary wave theory matches also the measured values in scenario 2 best, including both the maximum and mean water particle velocities, closely followed by the 5th order Stokes theory.

Taking into account the fit in terms of the surface elevation and the fluid kinematics, it is concluded that the higher order solitary wave theory is most appropriate in describing the observed landslide-tsunami in scenario 1 (solitary-like wave). In contrast, scenario 2 (Stokes-like waves) is best represented by the 5th order Stokes theory or alternatively by the stream function theory. Adopting these two most suitable theories (solitary and Stokes wave theories), Fig. 19 shows the wave kinematics over the crest regions. The solution for the particle velocity given in space by Munk (1949) is plotted over time in Fig. 19a thereby using $\Delta x = \Delta t \cdot c_{sol}$, with spacing Δx, time interval Δt = 1/15 s (inverse of the PIV frame rate) and

solitary wave speed c_{sol} = 1.99 m/s. A good overall agreement with the corresponding measurements in Fig. 14a,c is achieved for both scenarios.

5.2 Wave height prediction with energy flux conservation

This section explores the viability of predicting the wave heights in the intermediate geometries by energy flux conservation. Fig. 16 includes the relative wave heights H/h predicted by energy flux conservation in shallow water between section 1 (subscript 1) to section 2 (subscript 2)

$$H_2/H_1 = (h_1/h_2)^{1/4}(b_1/b_2)^{1/2} \quad . \tag{15}$$

Herein $h_1 = h_2$, such that the wave height for a new geometry at one particular location may be predicted by $H_2 = H_{2D}(b_{2D}/b_2)^{1/2}$, where H_1 is replaced by H_{2D}, the value measured in 2D at one particular location. The width in a new geometry approaches the curved crest with $b_2 = b_{2D} + 2r\theta\pi/180$. This simple energy flux conservation is based on the assumption that the tsunami is a linear wave and that the energy flux is constant with γ. The tsunamis may not necessarily have to be shallow-water waves in the present application of Eq. (15) as the water depth remains constant within a test. The predictions based on Eq. (15) are reasonably close to the simulated values for both θ = 7.5 and 15° (Fig. 16), and the agreement improves with increasing relative distance x/h. However, for $\theta \geq 30°$, Eq. (15) substantially underestimates the simulated wave heights, at least in scenario 1, and should not be applied. Better tsunami predictions based on Eq. (15) may be expected with known variation of the wave height with γ. Heller and Spinneken (2015) found for the 3D case $H_{3D} \propto \cos^{2\{1 + \exp[-0.2(r/h)]\}}(2\gamma/3)$, however, no such functions for intermediate geometries are currently available. Note that the findings of scenario 1 discussed herein are very similar to those of Heller et al. (2012). This is

not surprising, given that the dimensionless parameters of scenario 1 are close to those investigated in Heller et al. (2012). In contrast to this previous study, no significant scale effects are expected herein, and the findings are applicable to a wider range as two distinct scenarios have been investigated.

5.3 Implications on tsunami hazard assessment

The present study shows that DualSPHysics v3.1 has the real potential to be applied for realistic engineering problems, as already suggested by Crespo et al. (2011). In addition to advances in the numerical accuracy, this is greatly assisted due to reduced computational cost of the GPU acceleration and its user friendly pre- and post-processing tools. At present, the code may be particularly well suited to smaller water body geometries. However, this limitation is likely to be overcome in the near future. In the meantime, SPH may be coupled with a less computationally expensive wave propagation model, e.g. based on Boussinesq-type equations or other approaches (Narayanaswamy et al., 2010; Abadie et al., 2012; Altomare et al., 2014).

The two main aims of the numerical simulations were to support tsunami hazard assessment methods (i) (prediction with generic empirical equations) and (ii) (prediction with case-specific numerical simulations) in Section 1.1.2. The closely related work presented in HS15 enables the transformation of the 2D tsunami wave parameters from generic empirical equations to 3D. The numerical results in Figs. 15 and 16 support method (i), as these figures can be used to estimate the wave parameters in intermediate geometries between 2D and 3D. The presented results also demonstrate the significant potential of DualSPHysics to be used in method (ii), particularly for more energetic cases (scenario 1). Additional work and further development are required to exploit this full potential.

Generally, SPH simulations with DualSPHysics may result in slightly more accurate predictions for idealised geometries than generic empirical equations, as the latter typically exhibit a scatter of ±30% around their predictions. DualSPHysics may particularly be more reliable than generic empirical equations for complex water body geometries. In its application to practical examples, it is crucial that the simulations are thoroughly calibrated and validated. In the context of the present work, the slide velocity had to be reduced in the calibration procedure in order to reach a reasonable agreement between physical and numerical tests. Without this important step, the simulation would have considerably overestimated the tsunami amplitudes (Fig. 11).

6 Conclusions

Subaerial landslide-tsunamis were investigated adopting a composite (experimental-numerical) modelling approach. The primary aims were to provide enhanced physical insight into slide and wave kinematics and into the effect of the water body geometry, in order to extend the application range of existing generic empirical equations for preliminary landslide-tsunami hazard assessment. The geometrical effect was systematically quantified in a closely related study (Heller and Spinneken, 2015), with rigid slide tests conducted in a wave channel (2D, tsunami features change with the travel distance only) and a wave basin (3D, tsunami features change with the travel distance and direction). This revealed that waves in 2D may be up to a factor of 17 larger than in 3D. The present article investigated two of these 2D-3D test pairs in more detail namely a solitary-like wave propagating in h = 0.240 m deep water (weakly-dispersive, scenario 1) and Stokes-like waves in h = 0.480 m (strongly-dispersive, scenario 2).

6.1 Physical model tests

A set of very detailed measurements were obtained, including slide kinematics, fluid pressures, fluid velocities, water surface elevations and visual observations. The slide kinematics, combined with the measured fluid pressures, provided novel instantaneous slide-water interaction power graphs. These revealed that the majority of the energy is transferred within 0.5 s only, and that the pressure magnitude mostly depends upon the slide velocity. Potential and kinetic wave energies of the primary wave periods were also derived from the experimental data. Taken as a whole, the kinetic energy was found to be larger than the potential energy. Furthermore, 47% (scenario 1) and 18% (scenario 2) of the kinetic slide energy at the slide impact location was found to be transferred to the primary wave. The experimentally observed wave kinematics were also compared to 5^{th} order Stokes, 2^{nd} order cnoidal and higher order solitary wave theories as well as the stream function theory. Solitary wave theory most accurately predicts the wave kinematics of the solitary-like wave (scenario 1), and 5^{th} order Stokes theory most accurately describes Stokes-like waves (scenario 2).

6.2 Numerical model tests

The data of both scenarios were used to calibrate the smoothed particle hydrodynamics (SPH) open source code DualSPHysics v3.1, including a discrete element method to model the slide-ramp interaction. The numerical simulations were based on the same parameters as the physical model tests, except that the slide impact velocities were reduced. The simulated wave amplitudes in 2D slightly over-estimated the experimentally observed values, with maximum deviations of 10%. The corresponding 3D numerical amplitudes deviated by up to 35%. The main reason for these discrepancies lies in the challenge to appropriately model the slide kinematics. The modelling of the slide kinematics, water surface elevation and wave kinematics of the more energetic solitary-like wave (scenario 1) was more successful than that

of the less energetic Stokes-like waves (scenario 2). Five intermediate geometries, between 2D and 3D, were then addressed purely numerically. This included "channel" geometries with diverging side wall angles of θ = 7.5°, 15°, 30° and 45°, as well as the 3D corner case, with slide impact at the corner of the basin. For θ = 7.5°, the wave amplitudes along the slide axes lay approximately halfway between the values observed in 2D and 3D, and the values were practically identical to those in 3D for θ = 45°. This behaviour may not be predicted adequately with a simple shallow-water energy flux conservation. The above findings support hazard assessment, as wave parameters from generic empirical equations derived in 2D and 3D can now be translated to additional water body geometries. DualSPHysics was also found to be a convenient, yet somewhat more expensive, alternative to generic empirical equations. Most importantly, DualSPHysics is believed to allow for more accurate predictions in case-specific and complex geometries, provided the code is thoroughly validated and calibrated.

Future work aims to investigate the physical behaviour of landslide-tsunamis in more complex water body geometries involving larger domains and higher resolutions taking advantage of the GPU acceleration offered by DualSPHysics. The coupling of SPH simulations with a computationally less expensive wave propagation model is an alternative route towards reducing computational cost. Future work should involve the simulation and comparison of the pressure on the slide front, enabling a calibration of fluid-structure interaction problems. Additional real-world predictions should also be examined to further investigate the potential of DualSPHysics in supporting hazard assessment. Recently announced improvements by the DualSPHysics developers strongly support these aims, including double precision arithmetic and parallelisation of the GPU version. The improvement of the solid-solid interaction (slide kinematics) is ongoing, such that enhanced landslide-tsunami predictions may be expected in the near future.

Acknowledgement

The presented data are available upon request from the first author (Valentin.heller@nottingham.ac.uk) and scenario 1 is also published as a benchmark test case on the SPHERIC home page. This work was supported by the Natural Environment Research Council [Grant number NE/K000578/1]. The position of VH during this research project was funded by an Imperial College London Junior Research Fellowship (cohort 2011). The numerical simulations were conducted on the HPC facilities of Imperial College London. The great support of students and of the developers of DualSPHysics is also acknowledged.

Notation

a = wave amplitude, m;

b = channel width i.e. water body width, m;

b_s = slide width, m;

B = pre-factor in SPH pressure term $B = c_{0p}{}^2\rho_0/\gamma_p$, kg/(ms^2);

c = wave celerity, m/s;

c_{0p} = speed of sound at reference density, m/s;

c_p = speed of sound, m/s;

c_{sol} = solitary wave speed, m/s;

dp = initial distance between particles, mm;

E = energy, kgm^2/s^2;

f = scalar quantity associated with a SPH particle, various;

F = force, kgm/s^2;

F = slide Froude number F = $V_s/(gh)^{1/2}$;

g = gravitational acceleration g = 9.81, m/s^2;

g = vector due to gravity (0, 0, –g), m/s^2;

h = still water depth, m;

h_p = kernel smoothing length, m;

H = wave height, m;

l_s = slide length, m;

L = wave length, m;

m = mass, kg;

M = relative slide mass $M = m_s/(\rho_w b_s h^2)$;

p = pressure at a SPH particle, kg/(ms^2);

P = power, kgm^2/s^3;

r = radial distance from the slide impact zone, m;

r_{ijp} = distance between particles i and j;

R^2 = coefficient of determination;

s = slide thickness, m;

$\mathbf{s}$ = position vector at interpolation location of a SPH particle, m;

S = relative slide thickness $S = s/h$;

t = time (typically after slide impact), s;

t' = time shifted relative to slide impact, s;

T = wave period, s;

$\mathbf{u}$ = velocity vector of a SPH particle, m/s;

U = Ursell parameter $\mathsf{U} = HL^2/h^3$;

v_p = water particle velocity components based on PIV, m/s;

V_s = slide centroid impact velocity, m/s;

$\forall$ = volume, m^3;

W = smoothing kernel, $1/m^3$;

x = streamwise distance from the slide impact zone, m;

$\mathbf{x}$ = vector of integration position in SPH, m;

x' = coordinate along hill slope, m;

z = vertical coordinate, m;

α = slide impact angle i.e. hill slope angle, °;

δ = dynamic bed friction angle, °;

δ_p = delta parameter in SPH;

ΔE = energy for one time step, kgm^2/s^2;

Δt = time step, s;

Δz = height difference between slide centroid release and deposit position, m;

ε = constant to compute SPH particle velocity $\varepsilon = 0.5$;

ϕ = slide front angle, °;

γ = wave propagation angle, °;

γ_p = constant in SPH pressure expression $\gamma_p = 7$;

η = water surface elevation, m;

ν_0 = kinetic viscosity at laminar flow, m^2/s;

π = mathematical constant $\pi = 3.14159$;

Π = viscosity term, $m^5/(kgs^2)$;

θ = channel side wall angle, °;

ρ = density, kg/m^3;

ρ_0 = reference density, kg/m^3; and

Ω = SPH domain, m^3.

Subscript

f = front;

i, *j* = integer numbers referring to considered, neighbouring SPH particle;

kin = kinetic;

p = particle;

pot = potential;

s = slide;

w = water;

x,z = in *x*,*z*-direction;

1, 2 = section one, two; and

2D, 3D = 2D (wave channel), 3D (wave basin).

Abbreviation

BC = boundary condition;

CCD = charge-coupled device;

CFL = Courant-Friedrichs-Lewy;

CPU = central processing unit;

DEM = discrete element method;

GPU = graphical processing unit;

HPC = high performance computing;

HS15 = Heller and Spinneken (2015);

PIV = particle image velocimetry;

PVC = polyvinyl chloride;

SPH = smoothed particle hydrodynamics;

SWL = still water level;

VOF = Volume-of-Fluid;

2D, 3D = two-dimensional (wave channel), three-dimensional (wave basin); and

3Dc = three-dimensional (wave basin) with slide impact at corner.

References

Abadie, S.M., Harris, J.C., Grilli, S.T., Fabre, R., 2012. Numerical modeling of tsunami waves generated by the flank collapse of the Cumbre Vieja Volcano (La Palma, Canary Islands): tsunami source and near field effects. J. Geophys. Res. 117, C05030.

Abadie, S., Morichon, D., Grilli, S.T., Glockner, S., 2010. Numerical simulation of waves generated by landslides using a multiple-fluid Navier-Stokes model. Coast. Eng. 57 (9), 779–794.

Altomare, C., Crespo, A.J.C., Domínguez, J.M., Gómez-Gesteira, M., Suzuki, T., Verwaest, T., 2015. Applicability of Smoothed Particle Hydrodynamics for estimation of sea wave impact on coastal structures. Coast. Eng. 96 (2), 1–12.

Altomare, C., Suzuki, T., Domínguez, J.M., Crespo, A.J.C. Gómez-Gesteira, M., Caceres, I. 2014. A hybrid numerical model for coastal engineering problems. Proc. 34th Int. Conf. Coast. Eng., Seoul.

Antuono, M., Colagrossi, A., Marrone, S., 2012. Numerical diffusive terms in weakly-compressible SPH schemes. Comput. Phys. Commun., 183 (12), 2570–2580.

Ataie-Ashtiani, B., Nik-Khah, A., 2008. Impulsive waves caused by subaerial landslides. Environ. Fluid Mech. 8, 263–280.

Ataie-Ashtiani, B., Shobeyri, G., 2008. Numerical simulation of landslide impulsive waves by incompressible smoothed particle hydrodynamics. Int. J. Numer. Method Fluids 56 (2), 209–232.

Bascarini, C., 2010. Computational fluid dynamics modelling of landslide generated water waves. Landslides 7 (2), 117–124.

Battaglia, D., Strozzi, T., Bezzi, A., 2015. Landslide hazard: risk zonation and impact wave analysis for the Bumbuma Dam - Sierra Leone. Engineering Geology for Society and

Territory 2, Lollino, G., Giordan, D., Crosta, G., Corominas, J., Azzam, R., Wasowski, J., Sciarra, N. (Eds.), pp. 1129–1134, Springer, Basel.

BGC, 2012. Mitchell pit landslide generated wave modelling. Appendix 4-E, BGC Engineering Inc., Vancouver, BC, Canada.

Canelas, R., Ferreira, R.M.L., Crespo, A.J.C., Domínguez, J.M., 2013. A generalized SPH-DEM discretization for the modelling of complex multiphasic free surface flows. 8th International SPHERIC workshop, Trondheim, Norway.

Cannata, M., Marzocchi, R., Molinari, M.E., 2012. Modeling of landslide-generated tsunamis with GRASS. Trans. GIS 16 (2), 191–214.

Capone, T. , Panizzo, A., Monaghan, J.J. 2010. SPH modelling of water waves generated by submarine landslides. J. Hydr. Res. 48 (supplement 1), 80–84.

Chang, P., Melville, W.K., Miles, J.W., 1979. On the evolution of a solitary wave in a gradually varying channel. J. Fluid Mech. 95, 401−414.

Crespo, A.J.C., Domínguez, J.M., Barreiro, A., Gómez-Gesteira, M., Rogers, B.D., 2011. GPUs, a new tool of acceleration in CFD: efficiency and reliability on Smoothed Particle Hydrodynamics methods. PLoS ONE 6 (6), 1–13.

Crespo, A.J.C., Domínguez, J.M., Rogers, B.D., Gómez-Gesteira, M., Longshaw, S., Canelas, R., Vacondio, R., Barreiro, A., García-Feal, O., 2015. DualSPHysics: open-source parallel CFD solver based on Smoothed Particle Hydrodynamics (SPH). Comput. Phys. Commun. 187 (2), 204–216.

Crespo, A.J.C., Gómez-Gesteira, M., Dalrymple, R.A., 2007. Boundary conditions generated by dynamic particles in SPH methods. Computer, Material and Continua 5 (3), 173–184.

Cunningham, L.S., Rogers, B.D., Pringgana, G., 2014. Tsunami wave and structure interaction: an investigation with smoothed-particle hydrodynamics. Proceedings of the ICE - Engineering and Computational Mechanics 167 (3), 126–138.

Dalrymple, R.A., Rogers, B.D., 2006. Numerical modeling of water waves with the SPH method. Coastal Eng. 53 (2-3), 141–147.

Dean, R.G., 1965. Stream function representation of nonlinear ocean waves. J. Geophys. Res. 70 (18), 4561–4572.

Domínguez, J.M., Crespo, A.J.C., Valdez-Balderas, D., Rogers, B.D., Gómez-Gesteira, M., 2013. New multi-GPU implementation for Smoothed Particle Hydrodynamics on heterogeneous clusters. Comput. Phys. Commun. 184 (8), 1848–1860.

Fenton, J.D., 1985. A fifth-order Stokes theory for steady waves. J. Waterw. Port C-ASCE 111 (2), 216–234.

Fourtakas, G., Rogers B.D., Laurence D.R.P., 2013. Modelling sediment resuspension in industrial tanks using SPH. La Houille Blanche (2), 39–45.

Fritz, H.M., Hager, W.H., Minor, H.-E., 2004. Near field characteristics of landslide generated impulse waves. J. Waterw. Port C-ASCE 130 (6), 287–302.

Fuchs, H., Boes, R., 2010. Berechnung felsrutschinduzierter Impulswellen im Vierwaldstättersee. Wasser Energie Luft 102 (3), 215–221 (in German).

Fuchs, H., Pfister, M., Boes, R., Perzlmaier, S., Reindl, R., 2011. Impulswellen infolge Lawineneinstoss in den Speicher Kühtai. Wasserwirtschaft 101 (1-2), 54–60 (in German).

Fuchs, H., Winz, E., Hager, W.H., 2013. Underwater landslide characteristics from 2D laboratory modeling. J. Waterw. Port C-ASCE 139 (6), 480–488.

Fuhrman, D.R., Madsen, P.A., 2009. Tsunami generation, propagation, and run-up with a high-order Boussinesq model. Coast. Eng. 56 (7), 747–758.

Gingold, R.A., Monaghan, J.J., 1977. Smoothed particle hydrodynamics: theory and application to non-spherical stars. Mon. Not. R. Astron. Soc. 181 (3), 375–389.

Gómez-Gesteira, M., Rogers, B.D., Dalrymple, R.A., Crespo, A.J.C., 2010. State-of-the-art of classical SPH for free-surface flows. J. Hydraul. Res. 48 (supplement 1), 6–27.

Heinrich, P., 1992. Nonlinear water waves generated by submarine and aerial landslides. J. Waterw. Port C-ASCE 118 (3), 249–266.

Heller, V., 2007. Landslide generated impulse waves - prediction of near field characteristics. Ph.D. Thesis 17,531, ETH Zurich, Zurich.

Heller, V., Hager, W.H., 2010. Impulse product parameter in landslide generated impulse waves. J. Waterw. Port C-ASCE 136 (3), 145–155.

Heller, V., Hager, W.H., 2011. Wave types of landslide generated impulse waves. Ocean Eng. 38 (4), 630–640.

Heller, V., Hager, W.H., 2014. A universal parameter to predict subaerial landslide-tsunamis? J. Mar. Sci. and Eng. 2 (2), 400–412.

Heller, V., Hager, W.H., Minor, H.-E., 2008. Scale effects in subaerial landslide generated impulse waves. Exp. Fluids 44, 691–703.

Heller, V., Hager, W.H., Minor, H.-E., 2009. Landslide generated impulse waves in reservoirs - basics and computation. VAW-Mitteilung 211, R. Boes (Ed.), ETH Zurich, Zurich.

Heller, V., Moalemi, M., Kinnear, R.D., Adams, R.A., 2012. Geometrical effects on landslide-generated tsunamis. J. Waterw. Port C-ASCE 138 (4), 286–298.

Heller, V., Spinneken, J., 2013. Improved landslide-tsunami predictions: effects of block model parameters and slide model. J. Geophys. Res. 118 (3), 1489–1507.

Heller, V., Spinneken, J., 2015. On the effect of the water body geometry on landslide-tsunamis: physical insight from laboratory tests and 2D to 3D wave parameter transformation. Coast. Eng. 104 (10), 113-134.

Huber, A., Hager, W.H., 1997. Forecasting impulse waves in reservoirs. Proc., 19th Congrès des Grands Barrages, Florence, ICOLD, Paris, pp. 993–1005.

International Rivers, 2015. http://www.internationalrivers.org/programs/china (access 19.01.2015).

Jiang, L., LeBlond, P.H., 1994. Three-dimensional modeling of tsunami generation due to a submarine mudslide. J. Phys. Oceanogr. 24 (3), 559–572.

Kamphuis, J.W., Bowering, R.J., 1972. Impulse waves generated by landslides. Proc., 12th Coastal Engineering Conf. 1, ASCE, New York, pp. 575–588.

Keulegan, G.H., 1950. Wave motion. In: Rouse, H. (Ed.), Engineering Hydraulics. Wiley, New York, pp. 711–768.

Kranzer, H.C., Keller, J.B., 1959. Water waves produced by explosions. J. Appl. Phys. 30 (3), 398–407.

Li, Y., Raichlen F., 2003. Energy balance model for breaking solitary wave runup. J. Waterw. Port C-ASCE 129 (2), 47–59.

Liu, G.R., Liu, M.B., 2003. Smoothed particle hydrodynamics - a meshfree particle method. World Scientific, London.

Liu, P.L.-F., Wu, T.-R., Raichlen, F., Synolakis, C.E., Borrero, J.C., 2005. Runup and rundown generated by three-dimensional sliding masses. J. Fluid Mech. 536, 107–144.

Løvholt, F., Pedersen, G., Gisler, G., 2008. Oceanic propagation of a potential tsunami from the La Palma Island. J. Geophys. Res. 113, C09026.

Lynett, P., Liu, L.-F., 2005. A numerical study of the run-up generated by three-dimensional landslides. J. Geophys. Res. 110, C03006.

Mayrhofer, A., Rogers, B.D., Violeau, D., Ferrand, M. 2013. Investigation of wall bounded flows using SPH and the unified semi-analytical wall boundary conditions. Comput. Phys. Commun. 184 (11), 2515–2527.

Miller, D.J., 1960. Giant waves in Lituya Bay, Alaska. Geological survey professional paper No. 354-C, U.S. Government printing office, Washington, D.C.

Mohammed, F., Fritz, H.M., 2012. Physical modeling of tsunamis generated by three-dimensional deformable granular landslides. J. Geophys. Res. 117, C11015.

Molteni, D., Colagrossi, A., 2009. A simple procedure to improve the pressure evaluation in hydrodynamic context using the SPH. Comput. Phys. Commun. 180 (6), 861–872.

Monaghan, J.J., 1989. On the problem of penetration in particle methods. J. Comput. Phys. 82 (1), 1–15.

Monaghan, J.J., 1992. Smoothed Particle Hydrodynamics. Ann. Rev. Astron. Astr. 30, 543–574.

Monaghan, J.J., 1994. Simulating free surface flows with SPH. J. Comput. Phys. 110 (2), 399–406.

Monaghan, J.J., Kos, A., Issa, N., 2003. Fluid motion generated by impact. J. Waterw. Port C-ASCE 129 (6), 250–259.

Müller, L., 1964. The rock slide in the Vajont valley. Rock Mech. Eng. Geol. 2 (3-4), 148–212.

Munk, W.H., 1949. The solitary wave theory and its application to surf problems. Ann. NY Acad. Sci. 51, 376–424.

Narayanaswamy, M., Crespo, A.J.C., Gómez-Gesteira, M., Dalrymple, R.A., 2010. SPHysics-FUNWAVE hybrid model for coastal wave propagation. J. Hydraul. Res. 48 (supplement 1), 85–93.

Noda, E., 1970. Water waves generated by landslides. J. Waterway. Harbour. Coast. Eng. Div. ASCE 96 (WW4), 835–855.

Panizzo, A., De Girolamo, P., Petaccia, A., 2005. Forecasting impulse waves generated by subaerial landslides. J. Geophys. Res. 110, C12025.

Quecedo, M., Pastor, M., Herreros, M.I., 2004. Numerical modeling of impulse wave generated by fast landslides. Int. J. Numer. Methods Eng. 59, 1633–1656.

Rogers, B.D., Dalrymple, R.A., 2008. SPH modeling of tsunamis. In: Advances in coastal engineering: advanced numerical models for simulating tsunami waves and runup. Liu, P.L.-F., Yeh, H., Synolakis, C. (Eds.), chap. 3, pp. 75–100. World Scientific, Singapore.

Shao, S.D., Gotoh, H., 2005. Turbulence particle models for tracking free surfaces. J. Hydraul. Res. 43 (3), 276–289.

Slingerland, R.L., Voight, B., 1979. Occurrences, properties and predictive models of landslide-generated impulse waves. Rockslides and avalanches 2, Voight, B. (Ed.), Elsevier, Amsterdam, pp. 317–397.

St-Germain, P., Nistor, I., Townsend, R., Shibayama, T., 2014. Smoothed-particle hydrodynamics numerical modeling of structures impacted by tsunami bores. J. Waterw. Port C-ASCE 140 (1), 66–81.

Valdez-Balderas, D., Domínguez, J.M., Rogers, B.D., Crespo, A.J.C., 2013. Towards accelerating smoothed particle hydrodynamics simulations for free-surface flows on multi-GPU clusters. J. Parallel Distr. Com. 73 (11), 1483–1493.

Walder, J.S., Watts, P., Sorensen, O.E., Janssen, K., 2003. Tsunamis generated by subaerial mass flows. J. Geophys. Res. 108 (B5), 2236(2).

Ward, S.N., Day, S., 2003. Ritter Island Volcano - Lateral collapse and the tsunami of 1888. Geophys. J. Int. 154 (3), 891–902.

Watts, P., Grilli, S.T., Tappin, D.R., Fryer, G.J., 2005. Tsunami generation by submarine mass failure. II: predictive equations and case studies. J. Waterw. Port C-ASCE 131 (6), 298–310.

WCHL, 1970. Hydraulic model studies - wave action generated by slides into Mica Reservoir - British Columbia. Report, Western Canada Hydraulic Laboratories, Vancouver.

Wiegel, R.L., 1960. A presentation of cnoidal wave theory for practical application. J. Fluid Mech. 7 (2), 273–286.

Wiegel, R.L., Noda, E.K., Kuba, E.M., Gee, D.M., Tornberg, G.F., 1970. Water waves generated by landslides in reservoirs. J. Waterway. Harbour. Coast. Eng. Div. ASCE 96 (WW2), 307–333.

Wikipedia, 2015a. http://en.wikipedia.org/wiki/List_of_dams_and_reservoirs_in_Switzerland (access 16.07.2015).

Wikipedia, 2015b. http://en.wikipedia.org/wiki/List_of_Norwegian_fjords (access 16.07.2015).

Yim, S.C., Yuk, D., Panizzo, A., Di Risio, M., Liu, P.L.-F., 2008. Numerical simulations of wave generation by a vertical plunger using RANS and SPH models. J. Waterw. Port C-ASCE 134 (3), 143–159.

Zweifel, A., Hager, W.H., Minor, H.-E., 2006. Plane impulse waves in reservoirs. J. Waterw. Port C-ASCE 132 (5), 358–368.

Table 1. Physical model parameters of scenarios 1 and 2; note that the waves at all specified r/h and γ combinations were measured except at (r/h = 35.0; γ = 90°) in scenario 1 and at (15.0; 90°) and (22.5; 90°) in scenario 2.

Description	Symbol	Unit	Value scenario 1	Value scenario 2
Still water depth	h	(m)	0.240	0.480
Slide thickness	s	(m)	0.120	0.120
Slide width	b_s	(m)	0.577	0.577
Slide length	l_s	(m)	0.599	0.878
Slide front release position	x'	(m)	− 0.55 (2D), −0.47 (3D)	− 0.25 (2D and 3D)
Slide front impact velocity	V_{sf}	(m/s)	2.43 (2D), 2.23 (3D)	1.67 (2D), 1.73 (3D)
Slide centroid impact velocity	V_s	(m/s)	2.32 (2D), 2.33 (3D)	2.53 (2D), 2.46 (3D)
Dynamic bed friction angle	δ	(°)	12.7 (2D), 13.3 (3D)	11.1 (2D), 7.8 (3D)
Slide volume	~~V_s~~	(m^3)	0.038	0.057
Slide mass	m_s	(kg)	60.14	82.67
Slide density	ρ_s	(kg/m^3)	1597	1451
Water temperature	-	(°C)	21	21
Slide impact or hill slope angle	α	(°)	45	45
Slide Froude number	$F = V_s/(gh)^{1/2}$	(-)	1.51 (2D), 1.52 (3D)	1.17 (2D), 1.13 (3D)
Relative slide thickness	$S = s/h$	(-)	0.50	0.25
Relative slide mass	$M = m_s/(\rho_w b_s h^2)$	(-)	1.81	0.62
Channel width	b	(m)	0.600	0.600
Channel length	-	(m)	24.5	24.5
Unobstructed channel length	-	(m)	21.0	21.0
Basin length	-	(m)	12.0	12.0
Unobstructed basin length	-	(m)	7.4	7.4
Basin width	-	(m)	20	20
Relative wave probe distances in 2D	x/h	(-)	3.0, 5.0, 7.5, 10.0, 15.0, 22.5, 35.0	3.0, 5.0, 7.5, 10.0, 15.0, 22.5, 35.0
Relative wave probe distances in 3D	r/h	(-)	3.0, 5.0, 7.5, 10.0, 15.0, 22.5, 35.0	3.0, 5.0, 7.5, 10.0, 15.0, 22.5
Wave propagation angles in 3D	γ	(°)	0, 15, 30, 45, 58, 73, 90 (onshore run-up)	0, 15, 30, 45, 58, 73, 90 (onshore run-up)

Table 2. Formulations with the most relevant numerical parameters and constants used in DualSPHysics; *those values were only applied in the convergence tests.

Description	Unit	Selected value
Interaction kernel function	(-)	cubic spline
Time-stepping algorithm	(-)	velocity-Verlet
Viscosity formulation method	(-)	Artificial
Density filter	(-)	delta-SPH formulation
BCs	(-)	Dynamic
Initial distance between particles *dp*	(mm)	7.5*, 10, 15*
Real time simulation	(s)	2.5 (scenario 1), 2.28-3.2 (scenario 2)
CFL number	(-)	0.2
Coefficient of speed of sound	(-)	10
Smoothing length/particle size ratio h_p/dp	(-)	1.04
γ_p	(-)	7
ρ_0	(kg/m^3)	1000
ε	(-)	0.5
Frequency (number of time steps) application of Eulerian time stepping	(-)	40
Viscosity value ν_0	(m^2/s)	0.1
Delta-SPH coefficient (Antuono et al., 2012)	(-)	0.1
Initial/minimum time-step	(s)	$10^{-4}/10^{-5}$
Maximum/minimum allowed particle density	(kg/m^3)	1800/700
Young's modulus	(Pa)	$9 \cdot 10^7$
Poisson ratio	(-)	0.23
Bed friction coefficient	(-)	0.45

Table 3. Slide energies at impact and wave energies at different wave probe locations; *this value only includes the power observed for $t < 1$ s in Fig. 5f.

Quantity	Unit	Scenario 1	Scenario 2
Kinetic energy based on V_{sf}	(J)	177.6	115.3
Kinetic energy based on V_s	(J)	161.8	264.7
Upper slide energy limit given by $m_s g \Delta z$	(J)	468.5	747.4
Energy transferred from slide front to water body	(J)	123.3	112.6*
Potential wave energy at $x/h = 5.0$	(J)	-	24
Kinetic wave energy at $x/h = 5.0$	(J)	-	24
Total wave energy at $x/h = 5.0$	(J)	-	48
Kinetic/potential wave energy at $x/h = 5.0$	(-)	-	1.00
Potential wave energy at $x/h = 7.5$	(J)	33	21
Kinetic wave energy at $x/h = 7.5$	(J)	43	26
Total wave energy at $x/h = 7.5$	(J)	76	47
Kinetic/potential wave energy at $x/h = 7.5$	(-)	1.30	1.24
Potential wave energy at $x/h = 10.0$	(J)	35	21
Kinetic wave energy at $x/h = 10.0$	(J)	38	29
Total wave energy at $x/h = 10.0$	(J)	73	50
Kinetic/potential wave energy at $x/h = 10.0$	(-)	1.09	1.38
Potential wave energy at $x/h = 15.0$	(J)	36	-
Kinetic wave energy at $x/h = 15.0$	(J)	38	-
Total wave energy at $x/h = 15.0$	(J)	74	-
Kinetic/potential wave energy at $x/h = 15.0$	(-)	1.06	-

Table 4. Comparison of slide front impact velocities V_{sf} between the measured values in the physical experiments and the numerical values.

Description	Unit	Scenario 1	Scenario 2
2D physical experiment	(m/s)	2.43	1.67
2D numerical simulation	(m/s)	1.32	0.76
2D numerical/experimental value	(%)	54	46
3D physical experiment	(m/s)	2.23	1.73
3D numerical simulation	(m/s)	1.32	0.76
3D numerical/experimental value	(%)	59	44

Table 5. Comparison of measured, theoretical and simulated wave crest kinematics at x/h = 7.5 (scenario 1) and 5.0 (scenario 2); the mean water particle velocities are based on the values from the still water level SWL to the maximum crest elevation.

Method	**Scenario 1**		**Scenario 2**	
	Max. v_{px} (m/s)	Mean v_{px} (m/s)	Max. v_{px} (m/s)	Mean v_{px} (m/s)
Measured	1.21	0.97	0.37	0.36
5^{th} order Stokes	-	-	0.44	0.41
2^{nd} order cnoidal	-	-	0.48	0.45
Higher order solitary	1.25	0.99	0.40	0.39
Stream function	-	-	0.46	0.42
Numerical simulation	1.39	1.12	0.57	0.55

Fig. 1. Photograph of wave basin set-up in position 2, showing the medium slide on the ramp, the circular transition and steel plate at the ramp toe, side-walls with run-up probes and wave probes; note that the set-up was relocated for the measurements at γ = 0º, 15º (position 1) and at 58º, 73º and 90º (position 3) and the side-walls were extended in position 3.

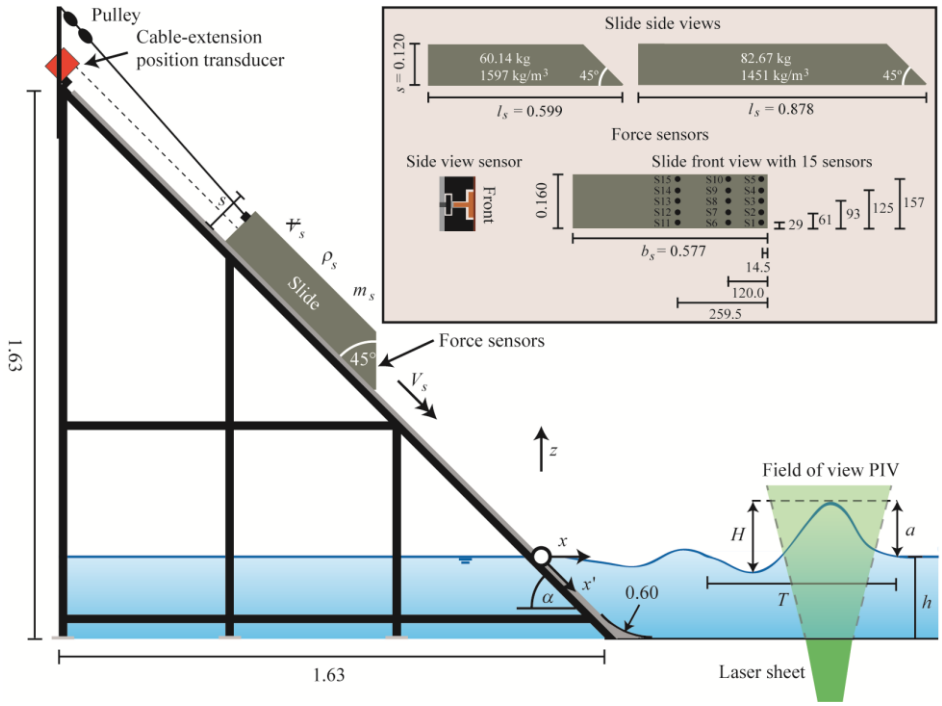

Fig. 2. Side view of set-up and measurement systems including slide properties and force sensor locations shown in the grey box; all length dimensions are in m except for the force sensor locations which are given in mm.

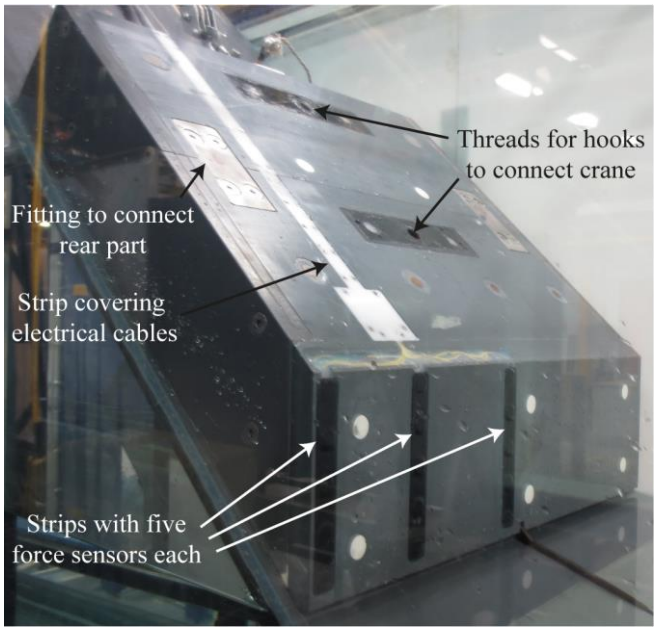

Fig. 3. Shorter slide in release position in 2D with slide front including 15 force sensors, white PVC strip to cover electrical cables, fittings to connect rear part and threads for the hooks to connect the overhead crane.

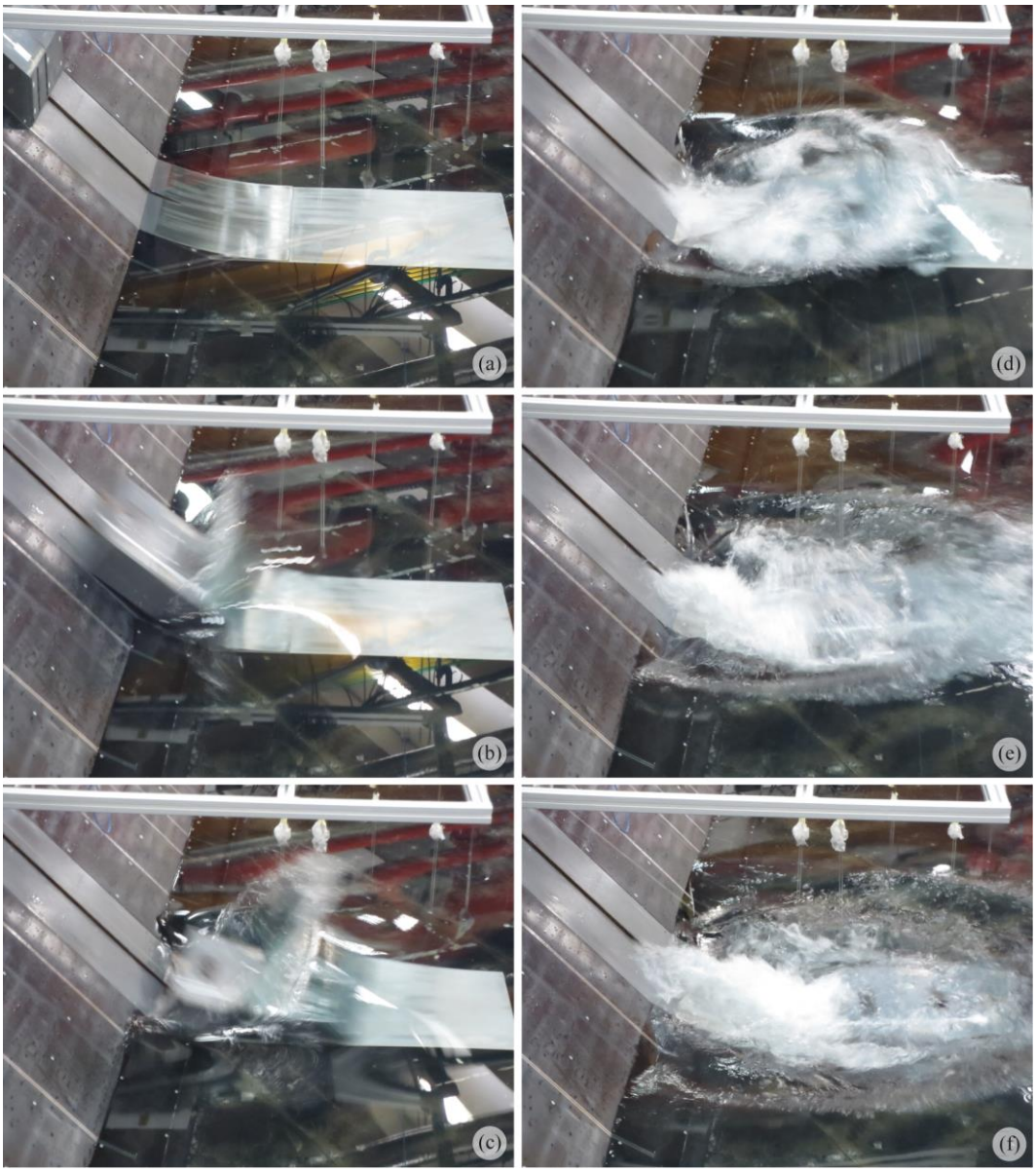

Fig. 4. Series of images of physical model tests with slide impact and tsunami generation in 3D for scenario 1; the time interval from (b) onwards is 0.2 s.

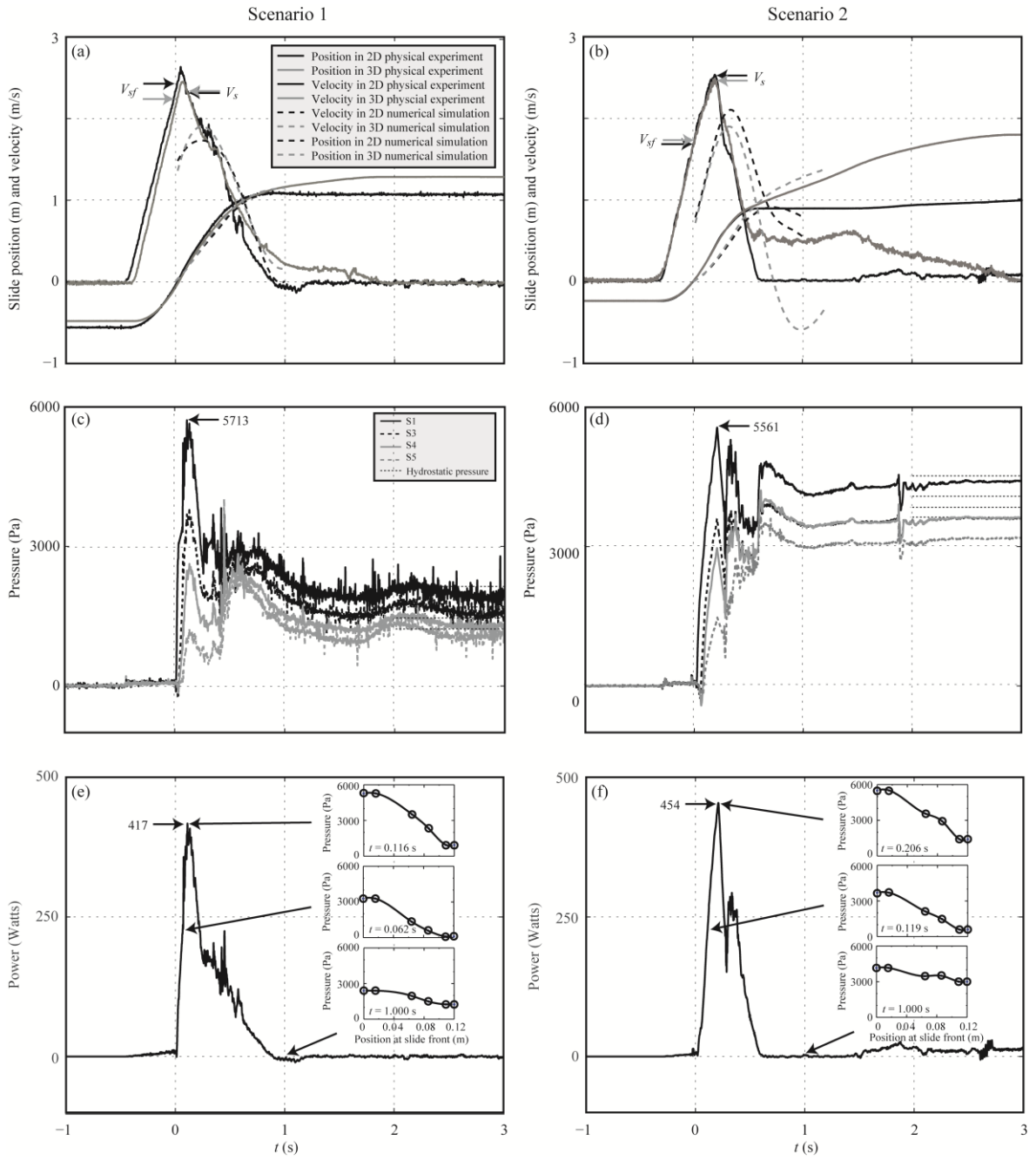

Fig. 5. Slide impact features versus time with t = 0 when slide nose reaches the still water surface: (a,b) measured and simulated positions and velocities for (a) scenario 1 and (b) scenario 2; (c,d) pressure on slide front in 2D measured with S1, S3, S4 and S5 (Fig. 2) for (c) scenario 1 and (d) scenario 2; (e,f) instantaneous slide-water interaction power $P(t)$ based on measurements on the slide front, with insets showing the pressure distributions over the slide front for three moments in time for (e) scenario 1 and (f) scenario 2.

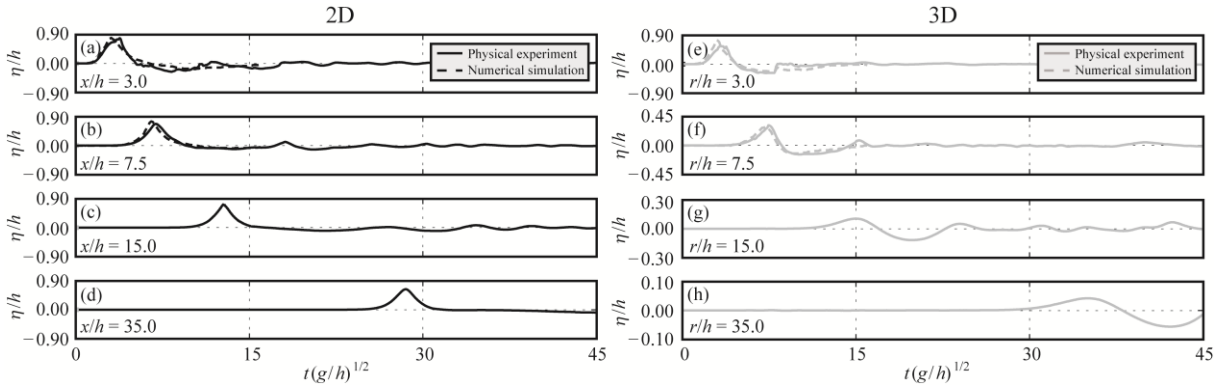

Fig. 6. Scenario 1: Comparison of relative water surface elevation η/h versus relative time $t(g/h)^{1/2}$ along the slide axis $\gamma = 0^{o}$ for $\mathsf{F} \approx 1.51$, $S = 0.50$ and $M = 1.81$ in both 2D (a-d) and 3D (e-h) at (a,e) $x/h = r/h = 3.0$, (b,f) 7.5, (c,g) 15.0 and (d,h) 35.0; note the increased scale on the ordinate in (f), (g) and (h).

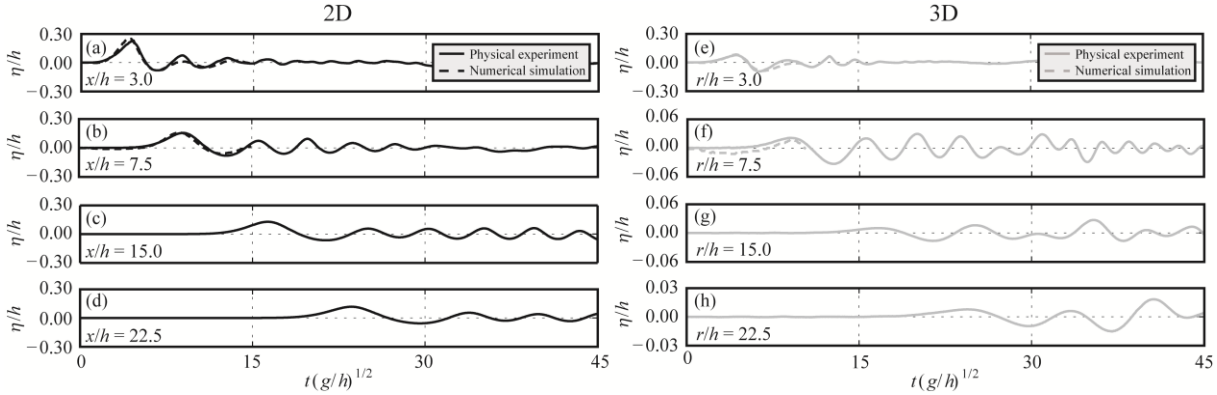

Fig. 7. Scenario 2: Comparison of relative water surface elevation η/h versus relative time $t(g/h)^{1/2}$ along the slide axis $\gamma = 0^{o}$ for $\mathsf{F} \approx 1.17$, $S = 0.25$ and $M = 0.62$ in both 2D (a-d) and 3D (e-h) at (a,e) $x/h = r/h = 3.0$, (b,f) 7.5, (c,g) 15.0 and (d,h) $x/h = r/h = 22.5$; note the increased scale on the ordinate in (f), (g) and (h).

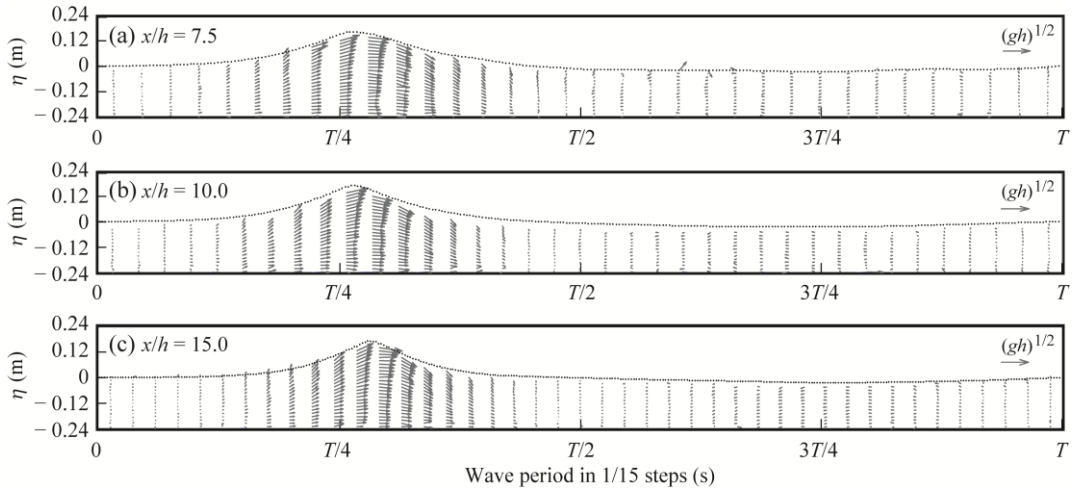

Fig. 8. 2D wave kinematics of scenario 1 measured with PIV over one wave period T relative to the linear shallow-water wave celerity $(gh)^{1/2}$ = 1.53 m/s at (a) x/h = 7.5 (T = 2.21 s), (b) 10.0 (2.41 s) and (c) 15.0 (2.82 s).

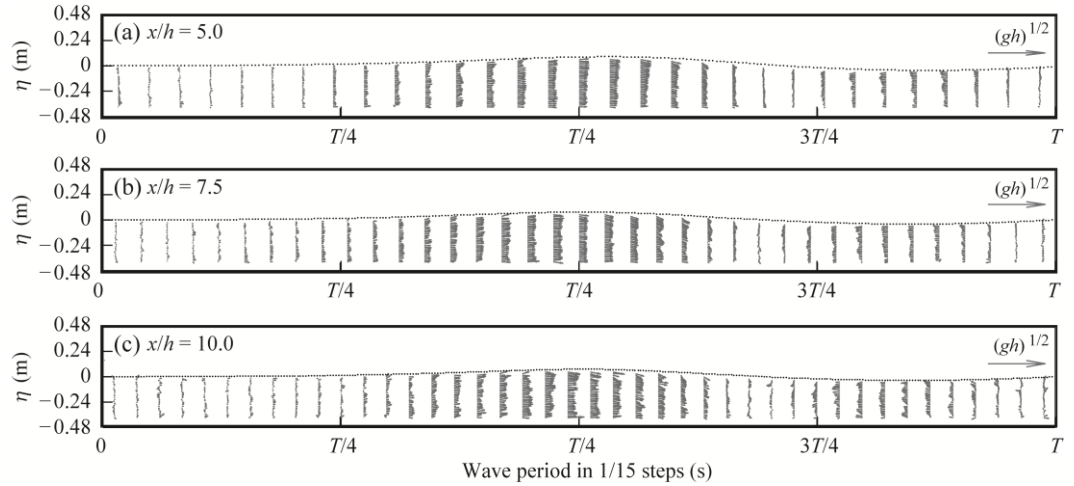

Fig. 9. 2D wave kinematics of scenario 2 measured with PIV over one wave period T relative to the linear shallow-water wave celerity $(gh)^{1/2}$ = 2.17 m/s at (a) x/h = 5.0 (T = 1.99 s), (b) 7.5 (2.38 s) and (c) 10.0 (2.71 s).

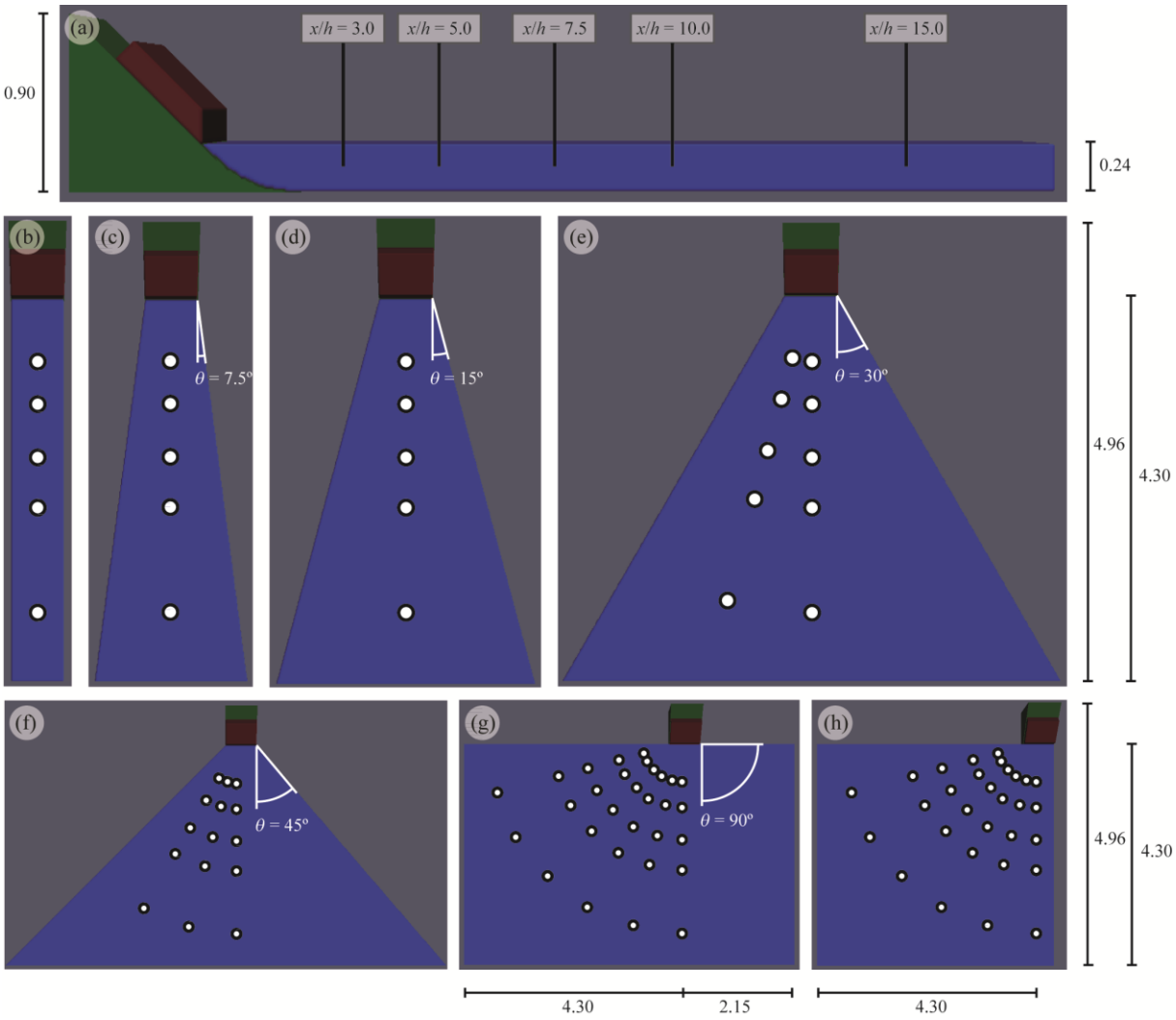

Fig. 10. Initial configurations in DualSPHysics of the seven investigated water body geometries with wave probe locations for scenario 1: (a) side view and (b) plan view of 2D case (channel side wall angle $\theta = 0^{o}$), (c) $\theta = 7.5^{o}$, (d) 15^{o}, (e) 30^{o}, (f) 45^{o}, (g) 3D case ($\theta = 90^{o}$) and (h) 3D corner case; the identical geometries were investigated in scenario 2 with an overall domain length of 6.76 m in 2D and 6.06 m in the remaining geometries rather than 4.96 m.

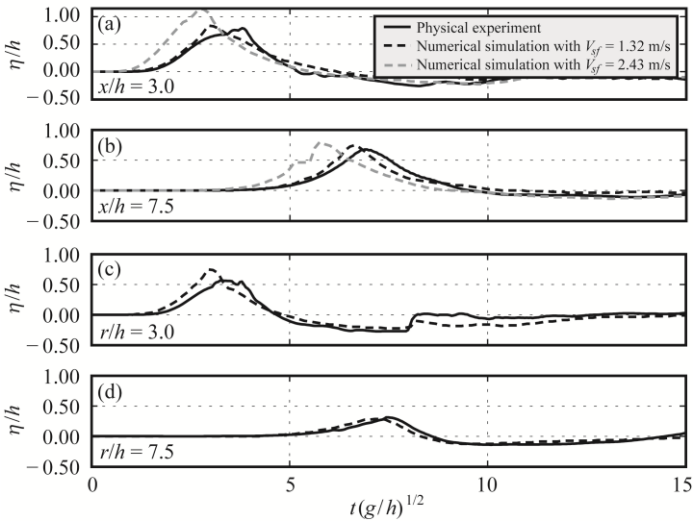

Fig. 11. Calibration (a,b) and validation (c,d) of numerical simulations of scenario 1 with wave profiles from physical experiments; relative water surface elevations η/h versus relative time $t(g/h)^{1/2}$ along the slide axis $\gamma = 0^{o}$ in 2D (a,b) and 3D (c,d) at (a,c) $x/h = r/h = 3.0$ and (b,d) 7.5; also shown are the numerical wave profiles for an unreduced slide impact velocity resulting in a considerable overestimation of the tsunami in (a).

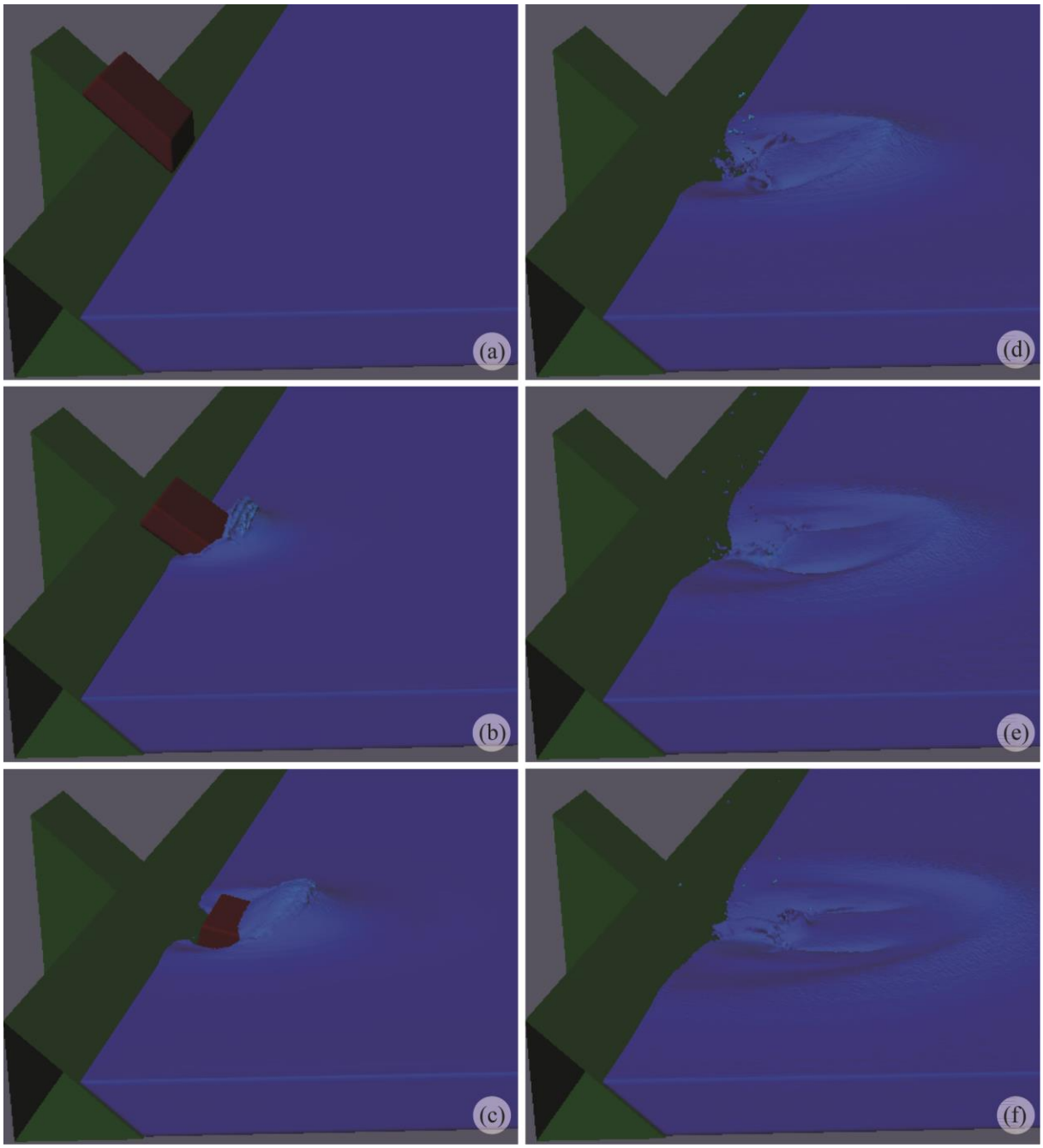

Fig. 12. Series of images from DualSPHysics of slide impact and tsunami generation of scenario 1 at identical time steps as shown in Fig. 4.

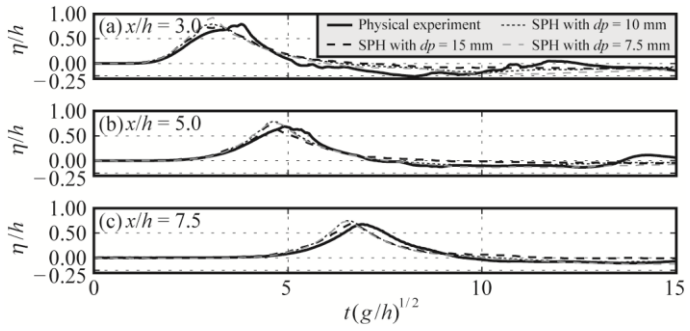

Fig. 13. Convergence tests with initial distance between particles dp = 7.5, 10 and 15 mm: relative water surface elevation η/h versus relative time $t(g/h)^{1/2}$ for scenario 1 in 2D at (a) x/h = 3.0, (b) 5.0 and (c) 7.5.

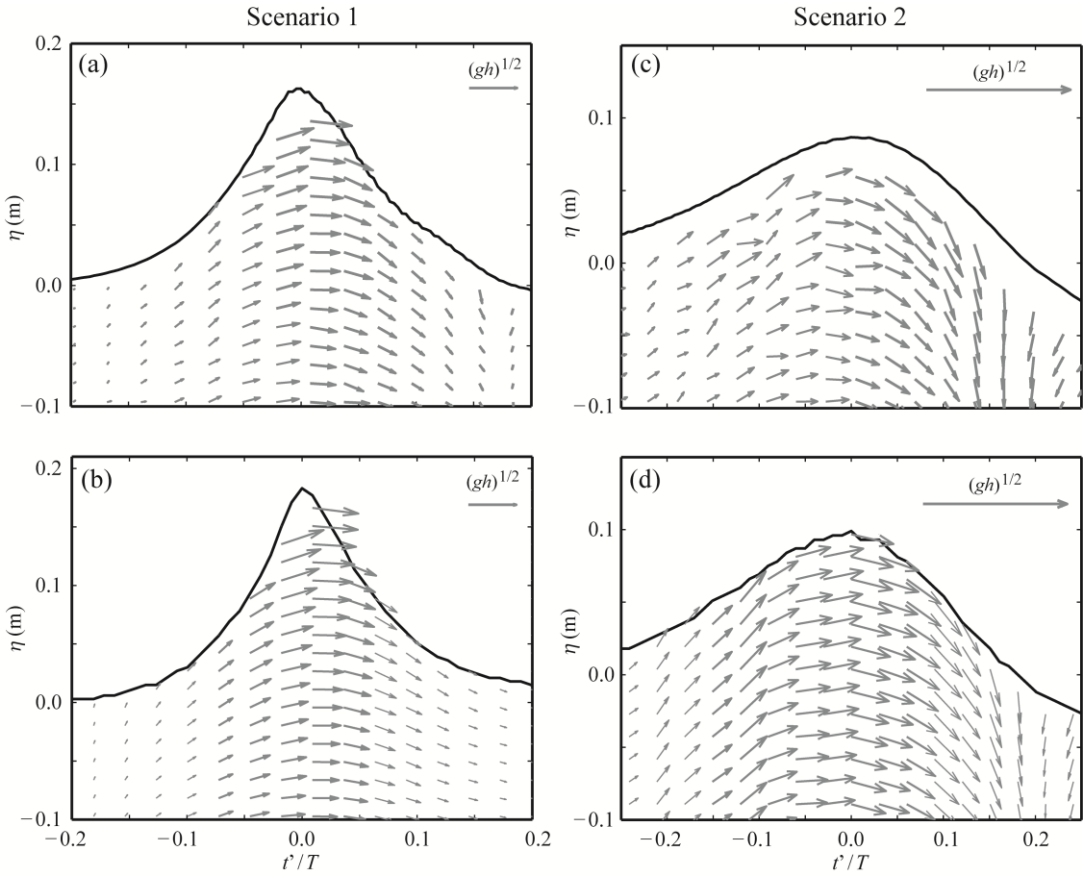

Fig. 14. 2D velocity vector field in the crest region measured with PIV and simulated with SPH: scenario 1 at x/h =7.5 from (a) PIV and (b) SPH and scenario 2 at x/h = 5.0 from (c) PIV and (d) SPH.

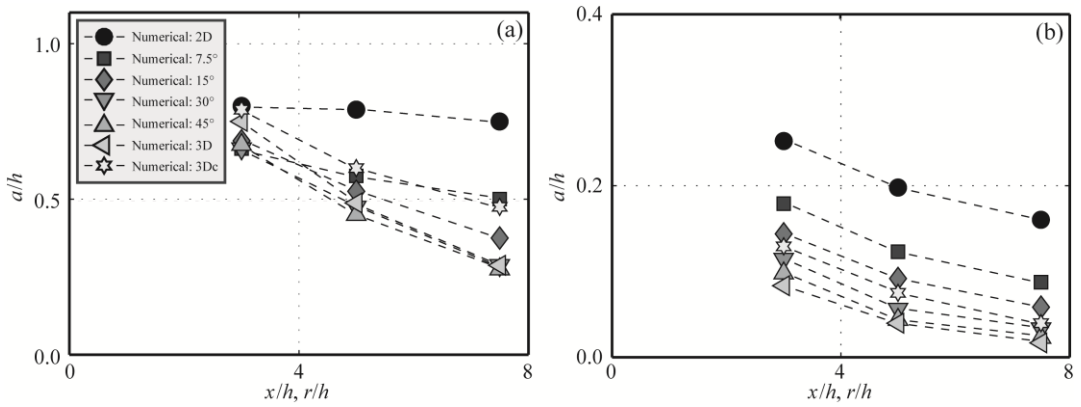

Fig. 15. Relative wave amplitude a/h along slide axis versus relative distance $x/h = r/h$ for all 7 cases of (a) scenario 1 and (b) scenario 2.

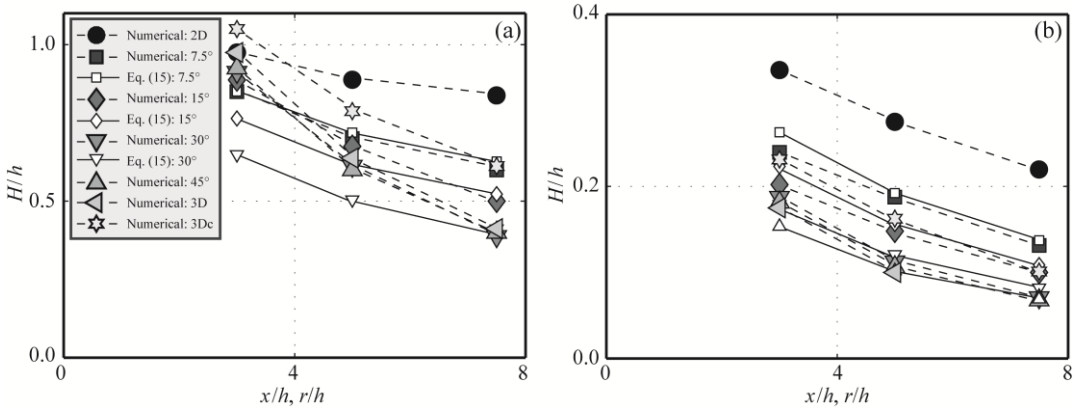

Fig. 16. Relative wave height H/h along slide axis versus relative distance $x/h = r/h$ for all 7 cases of (a) scenario 1 and (b) scenario 2.

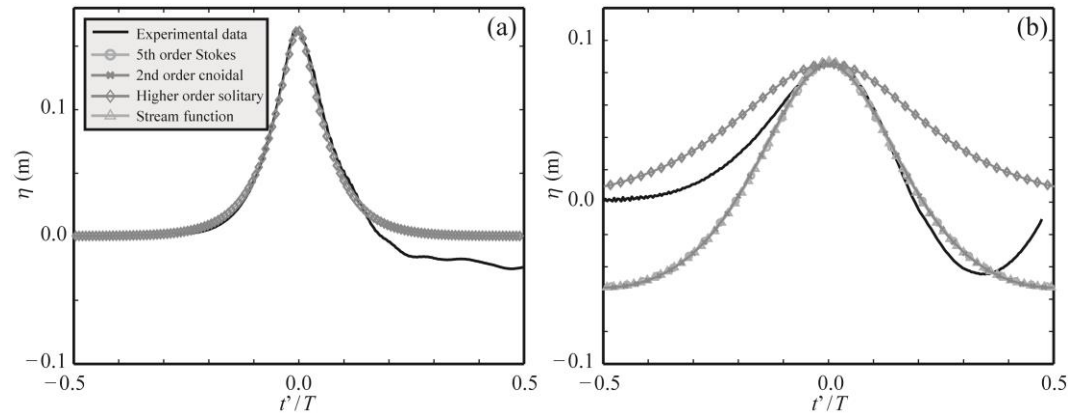

Fig. 17. Fit of theoretical to measured wave profiles over one experimentally measured wave period T; (a) scenario 1 at $x/h = 7.5$ and (b) scenario 2 at $x/h = 5.0$.

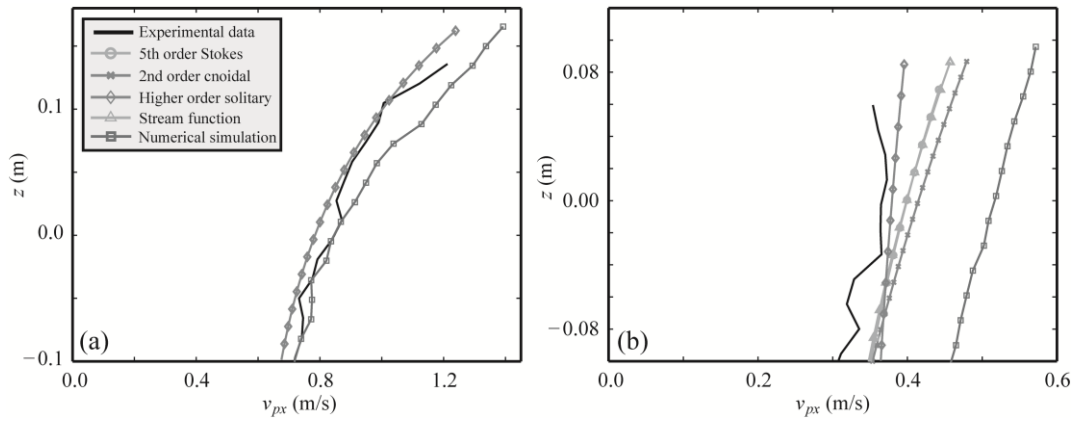

Fig. 18. Theoretical 2D water particle velocity distribution over depth below the wave crest based on the parameter settings found in the fits in Fig. 17; the theoretical profiles are compared to the measurements and simulations of (a) scenario 1 at x/h = 7.5 and (b) scenario 2 at x/h = 5.0.

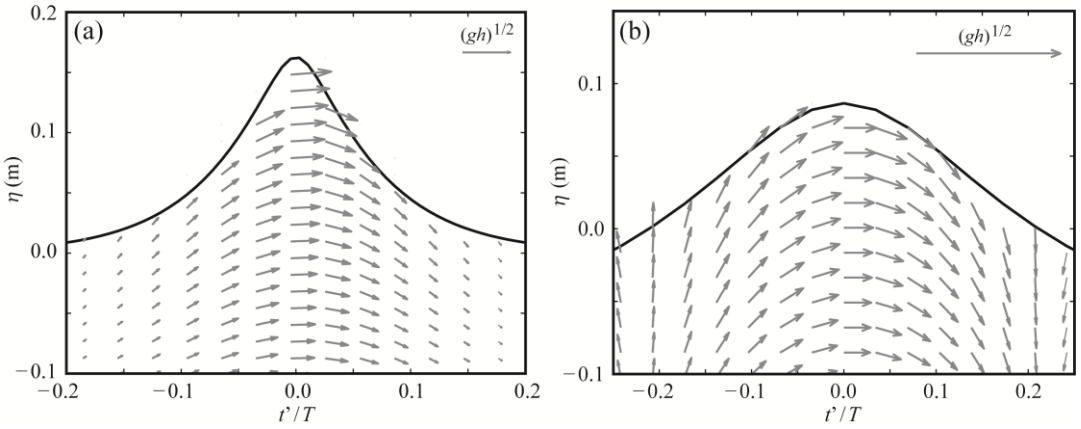

Fig. 19. 2D wave kinematics in the crest region based on the parameter settings found in the fits in Fig. 17 and predicted with the most appropriate wave theories; (a) higher order solitary wave theory for scenario 1 at x/h =7.5 and (b) 5th order Stokes wave theory for scenario 2 at x/h = 5.0.